*Sedimentology* (2008) **55,** 1717–1745 doi: 10.1111/j.1365-3091.2008.00965.x

# A three-dimensional numerical model of sediment transport, erosion and deposition within a network of channel belts, floodplain and hill slope: extrinsic and intrinsic controls on floodplain dynamics and alluvial architecture

DEREK KARSSENBERG* and JOHN S. BRIDGE†
**Department of Physical Geography, Faculty of Geosciences, Utrecht University, PO Box 80115, 3508 TC Utrecht, The Netherlands (E-mail: d.karssenberg@geo.uu.nl)*
†*Department of Geological Sciences, Binghamton University, PO Box 6000, Binghamton, NY 139002-6000, USA*

Associate Editor: Stephen Rice

**ABSTRACT**

A three-dimensional numerical model of sediment transport, erosion and deposition within a network of channel belts and associated floodplain is described. Sediment and water supply are defined at the upstream entry point, and base level is defined at the downstream edge of the model. Sediment and water are transported through a network of channels according to the diffusion equation, and each channel has a channel belt with a width that increases in time. The network of channels evolves as a result of channel bifurcation and abandonment (avulsion). The timing and location of channel bifurcation is controlled stochastically as a function of the cross-valley slope of the floodplain adjacent to the channel belt relative to the down-valley slope, and of annual flood discharge. A bifurcation develops into an avulsion when the discharge of one of the distributaries falls below a threshold value. The floodplain aggradation rate decreases with distance from the nearest active channel belt. Channel-belt degradation results in floodplain incision. Extrinsic (extrabasinal, allogenic) and intrinsic (intrabasinal, autogenic) controls on floodplain dynamics and alluvial architecture were modelled, and sequence stratigraphy models were assessed. Input parameters were chosen based on data from the Rhine–Meuse delta. To examine how the model responds to *extrinsic* controls, the model was run under conditions of changing base level and increasing sediment supply. Rises and falls in base level and increases in sediment supply occurred over 10 000 years. Rising base level caused a wave of aggradation to move up-valley, until aggradation occurred over the entire valley. Frequency of bifurcations and avulsions increased with rate of base-level rise and aggradation rate. Channel-belt width varied with water discharge and the lifespan of the channel belt. Wide, connected channel belts (and high channel-deposit proportion) occurred around the upstream inflow point because of their high discharge and longevity. Less connected, smaller channel belts occurred further down-valley. Such alluvial behaviour and architecture is also found in the Rhine–Meuse delta. During base-level fall, valley erosion occurred, and the incised valley contained a single wide channel belt. During subsequent base-level rise, a wave of aggradation moved up-valley, filling the incised valley. Bifurcation and avulsion sites progressively moved upstream. Relatively thin, narrow channel belts bordered and cut into the valley fill. These results differ substantially from existing sequence stratigraphy models. The increase in

 

sediment supply from upstream resulted in an alluvial fan. Most bifurcations and avulsions occurred at the fan apex (nodal avulsion), and channel belts were the widest and the thickest here (giving high channel-deposit proportion) due to their high discharge and longevity. The width and thickness of channel belts decreased down-valley due to decreased discharge, longevity and aggradation rate. This behaviour occurs in modern alluvial fans. *Intrinsic* controls also affect floodplain dynamics and alluvial architecture. Variation of aggradation rate, bifurcation frequency and number of coexisting channel belts occurred over periods of 500 to 2000 years, compared with 10 000 years for extrinsic controls. This variation is partly related to local aggradation and degradation of channel belts around bifurcation points. Channel belts were preferentially clustered near floodplain margins, because of low floodplain aggradation rate and topography there.

**Keywords** Alluvial architecture, alluvial fan, bifurcation, floodplain evolution, numerical modelling, process-based modelling.

## INTRODUCTION

Alluvial architecture is defined (Allen, 1978) as the geometry, proportion and spatial arrangement of channel-belt deposits within floodplain deposits. It has a fundamental control on the amount and movement of pore fluids (e.g. water and oil) in alluvial sedimentary successions. Quantitative, process-based (or process-imitating) models have been used since the late 1970s to help explain the influence of floodplain and channel geometry and dynamics on alluvial architecture, particularly variables such as channel-belt size relative to floodplain size, deposition rate, frequency and location of channel-belt avulsions (diversions), intrabasinal tectonic subsidence and compactional subsidence. The earliest quantitative models were two-dimensional, and considered alluvial architecture in vertical sections across floodplains normal to flow direction (Allen, 1978, 1979; Leeder, 1978; Bridge & Leeder, 1979; Bridge & Mackey, 1993a; Heller & Paola, 1996). The principles of these 2D models have also been used in fluvial sequence stratigraphy models to predict changes in near-coastal alluvial architecture in response to relative falls and rises in sea-level (Shanley & McCabe, 1993; Wright & Marriott, 1993). Despite the value of these early 2D models, they are too simplistic to apply confidently to a 3D alluvial succession.

The first 3D, quantitative, process-based model of alluvial architecture (Mackey & Bridge, 1995) allowed channel-belt avulsion to be treated as a function of flood discharge and the spatial and temporal distributions of floodplain topography, as controlled by the spatial and temporal distributions of channel-belt and floodplain deposition rate, intrabasinal tectonic subsidence and compactional subsidence. Although this model explained qualitatively many aspects of the dynamics of modern floodplains, it shared some important shortcomings of the 2D models, e.g.: (i) only one channel belt was active on the floodplain at a time; (ii) channel-belt geometry did not evolve through time; (iii) old channel belts could not be reoccupied by a later channel belt; (iv) sediment deposition and erosion in channel belts and across floodplains were not based on a mass balance of sediment input and output; (v) long-term channel-belt degradation and floodplain incision was not accounted for. These shortcomings make comparison of the models with real-world examples difficult and, in particular, establishment of the relative roles of extrinsic (extrabasinal, allogenic) and intrinsic (intrabasinal, autogenic) factors in controlling floodplain dynamics and 3D alluvial architecture.

Extrinsic controlling factors originate outside the alluvial plain, and include regional climate, extrabasinal tectonic activity (both of which control water and sediment supply to the alluvial plain) and base-level change. Extrinsic factors therefore control the boundary conditions of a model that influence floodplain dynamics and alluvial architecture. Extrinsic controlling factors can vary over periods of up to millions of years and cause variations in alluvial architecture over sediment thicknesses of metres to kilometres (Bridge, 2003). Intrinsic controlling factors originate within the alluvial plain, and result from the floodplain processes and their interaction (such as floods and avulsion). Intrinsic controlling factors cause random or cyclic variation in floodplain dynamics and alluvial architecture.

Intrinsic cyclic variations in floodplain dynamics can have periods of hundreds to thousands of years and cause variations in alluvial architecture over sediment thicknesses of metres to hundreds of metres (Bridge, 2003). Extrinsic and intrinsic factors are difficult to differentiate because they have overlapping periods, and because extrinsic factors influence intrinsic factors (Bridge, 2003; Stouthamer & Berendsen, 2007).

Driven by the shortcomings of pre-existing models, Karssenberg *et al.* (2003) and Karssenberg & Bridge (2005) have substantially modified and developed the Mackey–Bridge approach, particularly the component models for aggradation and degradation, avulsion, and the development of channel belts following avulsion. Such development has been made possible, in part, by the availability of new data from modern floodplains, especially the Holocene Rhine–Meuse delta. Channel-belt aggradation and degradation are calculated using the sediment continuity equation, and are therefore controlled by input and output of sediment to the alluvial system. Floodplain aggradation is a function of channel-belt aggradation rate and distance from channel belts, and floodplain degradation is treated using a sediment diffusion–advection approach. Depending on flood discharge and the ratio between channel-belt slope and transverse floodplain slope, new channel belts are formed by channel bifurcation, and multiple channel belts may develop and coexist (forming distributive and anastomosing rivers). In some cases, a pre-existing channel belt is abandoned in favour of another one, and an avulsion occurs. Following bifurcation and avulsion, the width of a new channel belt increases progressively as channel migration proceeds in the channel belt. During degradation, upstream migration of knick points and formation of incised channels and terraces can be simulated. The effect of cyclic variation in degradation and aggradation on floodplain dynamics and alluvial architecture can be simulated, allowing a link to sequence stratigraphic models.

The purpose of this paper was to: (i) present the details of the new model; (ii) explore how intrinsic and extrinsic factors affect floodplain dynamics (e.g. aggradation, degradation, evolution of the channel network by bifurcation and avulsion) and alluvial architecture; (iii) qualitatively compare model outputs with real-world data, especially from the Holocene Rhine–Meuse delta; and (iv) evaluate model behaviour for a wide range of parameter values by executing a sensitivity analysis.

## MODEL DESCRIPTION

### Modelling area and time period

The rectangular modelling area has down-valley length $l$ (m) and width $w$ (m), and is discretized by square raster cells with constant cell length $c_l$ (m). The cell centre coordinates $x$, $y$ (m) have an origin at the bottom left corner of the modelling area, and represent the lateral and downstream directions respectively. Each cell has surface elevation $h$ (m). The initial floodplain surface is assumed in the scenarios presented here to have a constant slope with additional small random noise, calculated as:

$$h = s_f y + u(0,e) \quad (1)$$

in which $s_f$ is the initial downstream floodplain slope, $u(0,e)$ (m) is a realization of a stochastic variable having a uniform distribution between zero and $e$. The model discretizes time ($t$) in time steps with duration $\Delta t$ (years), with a start time $t_{st}$ (years) and end time $t_{end}$ (years). The time-step duration used here is $\Delta t = 1$ year.

### Network of channels, water discharge and transport of sediment

Water flow and sediment transport occur through a network of channels, where each channel represents aggregated water flow and sediment transport of a channel belt. This channel network consists of lines (channels) connected to each other at bifurcation or convergence points (Fig. 1). Each channel consists of a set of arcs connecting centres of neighbouring raster cells. The channel network is fed with water and sediment by a single channel that enters the modelling area at a fixed position at the upstream edge, referred to as the inflow point (Fig. 1). A variable amount of water ($Q_w$, $m^3\ year^{-1}$) enters the channel network at the inflow point and flows in a down-slope direction through the channel network, assuming zero addition or subtraction of water in the modelling area. The amount of water discharge for each channel in the network is $q_w$ ($m^3\ year^{-1}$). As the time step is much larger than the travel time of water through the modelling area, all water that enters the modelling area at a certain time step leaves the modelling area at the same time step.

 

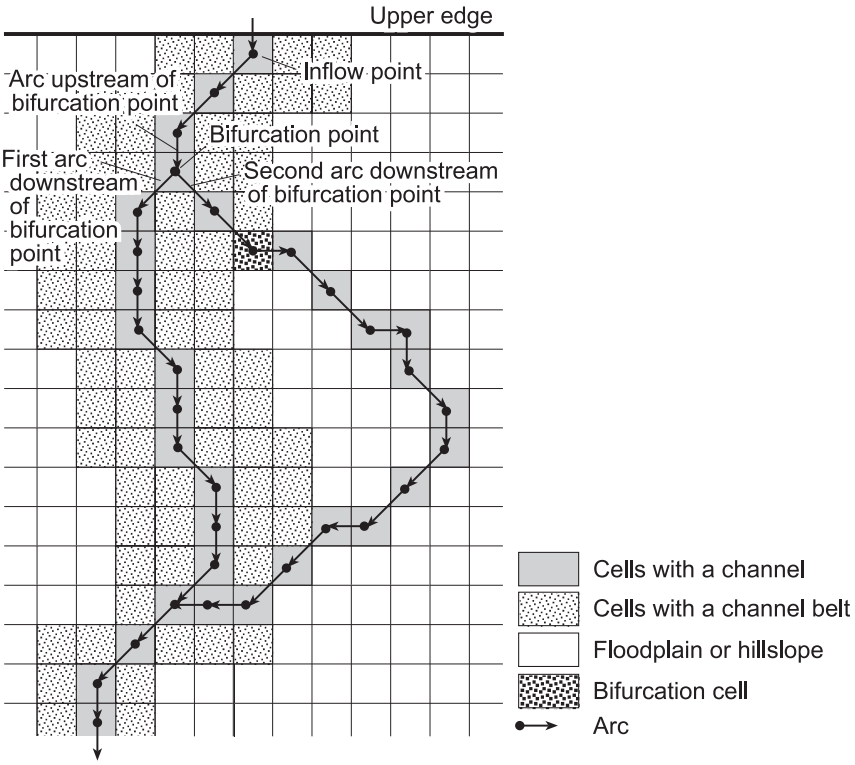


**Fig. 1.** Cellular representation of channels, channel belts and floodplain or hill slope areas in the model. Only the upper part of the modelling area is shown. The situation is shown just after a bifurcation of a channel to the right on the figure. In this case, the bifurcating channel rejoins the other channel down-valley, but it may also flow downhill to the lower edge of the modelling area.

One-dimensional sediment transport ($q_s$, $m^3$ $year^{-1}$) through a channel is:

$$q_s = -aq_w \frac{\partial h}{\partial x_c} \quad (2)$$

in which $a$ is a dimensionless parameter, $x_c$ is downstream distance (m) along the channel, calculated as the length of the arcs connecting channel cells (Fig. 1), $h$ is elevation (m) of the bank of the channel which equals the floodplain surface elevation. Sediment transport in Eq. 2 includes bedload and suspended load. This equation applies to a single mean grain-size, dependent on the parameter $a$. Equation 2 does not include an entrainment threshold term because it is assumed that most sediment transport occurs at flood stage when stream power is orders of magnitude greater than the threshold stream power. Other sediment transport laws could be used, but this was not carried out here, for simplicity. The sediment transport $q_s$ refers to solid sediment plus pore space, just like all other sediment transport terms and sediment inputs referred to in this paper. The mass balance for the channel system is aggregated over the channel-belt width:

$$\frac{\partial h}{\partial t} w_{cb} = i + \frac{\partial q_s}{\partial x_c} \quad (3)$$

in which $w_{cb}$ (m) is the width of the channel belt, calculated with equations provided below, and $i$ ($m^2$ $year^{-1}$) is the sediment input from hill slopes to the channel ($m^2$ $year^{-1}$), calculated using the hill slope degradation module described in a later section. The width of the channel belt and the sediment and water supply to the channel belt also vary with time; however, their derivatives with respect to time are so small that they can be ignored. Combining Eqs 2 and 3 gives:

$$\frac{\partial h}{\partial t} w_{cb} = i - \frac{\partial}{\partial x_c}\left(aq_w \frac{\partial h}{\partial x_c}\right) \quad (4)$$

Equation 4 is solved with two boundary conditions. At the inflow point at the top of the channel network, $q_s$ equals $Q_s$, which is the variable channel-belt sediment input to the modelling area. At the bottom of the modelling area, $h$ of the channel network is set to $H$, which is the variable base level (m). Equation 4 is solved numerically for each time step for all channel arcs on the channel network using an explicit solution. For each arc, this solution uses its associated channel-belt width ($w_{cb}$) calculated according to the equations below.

## Channel and channel-belt geometry

As purely physically based equations for channel and channel-belt geometry do not yet exist, equations are used that are derived from

quasi-physically based approaches with parameters estimated from a large data set of geometries of channels from various rivers. The following variables are calculated for each arc of the channel network and for each time step. Bankfull channel width ($w_c$, m) is (from Singh *et al.*, 2003a,b):

$$w_c = 0{\cdot}50z\frac{(jq_w)^{0{\cdot}462}}{s_{par}^{0{\cdot}231}} \quad (5)$$

in which $j$ is a conversion constant $m^3$ $year^{-1}$ to $m^3$ $sec^{-1}$, $s_{par}$ is the topographical slope of the arc and $z$ is the channel side slope, which is assumed to be constant and the same for all channel cells. Bankfull mean flow depth ($d$, m) is (from Singh *et al.*, 2003a,b):

$$d = 1{\cdot}52\left(\frac{n}{z}\right)^{0{\cdot}6} z\frac{(jq_w)^{0{\cdot}323}}{s_c^{0{\cdot}161}} \quad (6)$$

in which $n$ is Manning's $n$ (s $m^{-1/3}$). For each arc, the maximum width ($m$, m) of the associated channel belt at that location is (Bridge & Mackey, 1993b; Bridge, 2003):

$$m = 59{\cdot}86d^{1.8} \quad (7)$$

For arcs of a newly formed channel (with a zero age), the associated channel-belt width ($w_{cb}$, m) is:

$$w_{cb} = w_c \quad (8)$$

For arcs of channels with an age greater than zero years, the change in the channel-belt width is:

$$\frac{\partial w_{cb}}{\partial t} = c(m - w_{cb}) \quad (9)$$

in which $c$ is the bank erodibility ($year^{-1}$). For reasons of simplicity, and because of the difficulties in estimating values of $c$ as a function of bank material (Gouw & Berendsen, 2007; Makaske *et al.*, 2007), $c$ is assumed to be constant. Equation 9 is solved for each arc and each time step using an explicit numerical solution. Although the channel-belt width increases through time, the channel belt does not gradually migrate laterally by bank erosion.

For each time step, the area containing a channel belt is calculated as the area consisting of all cells with a distance to the nearest arc less than the $w_{cb}$ value of that arc. For each time step, the topographical height ($h$, m) of these channel-belt cells equals the topographical height of the nearest arc, as calculated by Eq. 4. In addition, the level of the erosional surface of the channel belt for these channel-belt cells is calculated using the value of the flow depth ($d$, Eq. 6) of the nearest arc.

## Bifurcation and avulsion

Comprehensive, physically based models for channel-belt bifurcations and avulsions do not exist at present. The models adopted here build upon the previous work of Mackey & Bridge (1995), Slingerland & Smith (1998) and Sun *et al.* (2002). Meijer (2002) and Overeem *et al.* (2005) have also attempted to numerically model avulsions in fluvial-coastal cellular models, but details of these avulsion models were not provided. The possibility of the occurrence of a bifurcation is simulated for each time step as a random function of super-elevation of the channel belt, under the condition that a high flood discharge occurred during that time step. This flood discharge condition is evaluated first. For each time step, the event $D$ of a maximum yearly flood discharge possibly leading to a bifurcation occurs with a constant probability $P(D)$. A realization $D$ is drawn for each time step. If $D$ is FALSE for a certain time step, the flood discharge was too low and no bifurcation occurred during that time step. If $D$ is TRUE, flood discharge was sufficiently high for a bifurcation to occur, but only when super-elevation of the channel belt is sufficiently high. The effect of super-elevation is represented by calculating the probability of a bifurcation given a high flood discharge $P(B)$ for each cell at the edge of a channel belt, for each current time step:

$$P(B) = \min((\kappa r_s)^{\mu}, 1) \quad (10)$$

in which $r_s$ is the slope ratio, $\kappa$ and $\mu$ are parameters, and the function $\min((\kappa r_s)^{\mu}, 1)$ is evaluated to the minimum value of $(\kappa r_s)^{\mu}$ and 1. The value of $r_s$ is calculated as:

$$r_s = \frac{\max(s_{per}, 0)}{s_{par}} \quad (11)$$

where $s_{per}$ is the slope in the direction perpendicular away from the channel belt, $s_{par}$ is the slope of the channel in the nearest cell containing the channel associated with the channel belt and the function $\max(s_{per}, 0)$ is evaluated to the maximum value of $s_{per}$ and 0. The value of $s_{per}$

is calculated from the topographical height ($h$) of cells in a $3 \times 3$ window of cells centred around the cell under consideration neighbouring a channel belt, using the third-order finite-difference method of Horn (1981).

If $D$ is TRUE, a realization of $B$ is drawn for each cell at the edge of a channel belt. If $B$ at a cell is TRUE also, a bifurcation occurs at the corresponding cell, referred to as the bifurcation cell (Fig. 1). If $B$ is FALSE no bifurcation occurs. If $D$ is TRUE and $B$ is TRUE at more than one cell in the same time step, a bifurcation occurs at the cell with the highest value of $P(B)$ only, to prevent the occurrence of more than one bifurcation at a single time step. As shown in Fig. 1, the new channel consists of two segments. The first segment, upstream of the bifurcation cell, connects the bifurcation cell with the older channel, resulting in the bifurcation point, which is the actual location of the bifurcation (Fig. 1). The second segment, downstream of the bifurcation cell, consists of a set of arcs extending from the bifurcation cell and connecting cells in the direction of the locus of maximum downhill topographical slope calculated with the eight-point pour algorithm (Moore, 1996; Burrough & McDonnell, 1998). The end of the new channel is either the bottom of the modelling area or a location where it meets and flows into another channel.

At bifurcations, water is distributed over the two bifurcating channels (following Murray & Paola, 1994; Sun *et al.*, 2002) according to:

$$\left.\begin{array}{l} \dfrac{q_1}{q_2} = \dfrac{\sqrt{s_1 n_1(1,\sigma^2)}}{\sqrt{s_2 n_2(1,\sigma^2)}} \\ q_0 = q_1 + q_2 \end{array}\right\} \qquad (12)$$

in which $q_1$ and $s_1$ are, respectively, the discharge ($m^3$ $year^{-1}$) and gradient of the first bifurcating channel, $q_2$ and $s_2$ are the same variables for the second bifurcating channel, and $q_0$ is the discharge ($m^3$ $year^{-1}$) of the channel upstream of the bifurcation point. The gradient $s_1$ is calculated from the surface elevation ($h$) at the cell corresponding to the bifurcation point and the surface elevation ($h$) at the cell directly downstream of the bifurcation point, on the first bifurcating channel. $s_2$ is calculated in the same way for the second bifurcating channel. Each of the values $n_1(1, \sigma^2)$ and $n_2(1, \sigma^2)$ are independent realizations of a random variable with a normal distribution with mean zero and variance $\sigma^2$ and are drawn at each time step. These noise terms are included to represent local random effects on channel gradients at the bifurcation point.

After a bifurcation has formed, the model determines for each time step what happens with the bifurcation, either: (i) the bifurcation continues to exist; (ii) the bifurcation develops into an *avulsion*, whereby the older channel downstream of the bifurcation point is removed, while the new channel downstream of the bifurcation point continues to exist; or (iii) the more recent channel downstream of the bifurcation point is removed, while the older channel downstream of the bifurcation point remains, referred to as an *unsuccessful bifurcation*. To decide which of the three options applies for a specific bifurcation, the model calculates the discharge ratios $u_1$ and $u_2$ for each time step and for each bifurcation:

$$u_i = \frac{q_i}{q_0} \qquad (13)$$

for $i$ equals 1 and 2, respectively, the first and second bifurcating channel downstream of the bifurcation point. When $u_1$ or $u_2$ drops below $u_{crit}$, the critical discharge ratio, the channel downstream of the bifurcation point with the lowest discharge is removed, corresponding to an avulsion or unsuccessful bifurcation, depending on which channel is removed. For $u_i$ values above $u_{crit}$, the bifurcation remains. Note that the removal of one of the two channels downstream of a bifurcation implies the removal of all channels and bifurcations downstream of this point receiving discharge from this channel only. A downstream bifurcation removed in this way is referred to as a *removed inflow channel bifurcation*.

Factors other than the maximum flood discharge and super-elevation of the channel belt (i.e. slope ratio), such as bank erodibility and the proximity of pre-existing channels, can also influence the probability of avulsion (e.g. Aslan *et al.*, 2005). These factors are not considered explicitly here, but can partly be accounted for by the probabilistic nature of Eq. 10. The dependence of avulsion probability on super-elevation of the channel belt (i.e. slope ratio) means that the frequency of avulsion depends on the channel-belt aggradation rate, as has been found in experimental studies (Bryant *et al.*, 1995; Ashworth *et al.*, 2004, 2007).

## Floodplain aggradation and hill slope degradation

Floodplain aggradation is not incorporated in the mass balance of the channel belt. The amount of floodplain aggradation is modelled to be

dependent on the aggradation rate of the channel belt, under the assumption that sufficient sediment is available. For a cell not belonging to the channel belt, floodplain aggradation occurs only when its topographical elevation ($h$) is less than the topographical elevation ($h$) of the nearest channel-belt cell. If this is the case, floodplain aggradation rate ($g$, m year$^{-1}$) of the cell is calculated for each time step as (from Karssenberg *et al.*, 2001):

$$g = g_c C + g_c(1 - C)e^{-d_c/b} \quad (14)$$

in which $g_c$ is the aggradation rate (m year$^{-1}$) at the nearest channel-belt cell, $C$ is a fraction of $g_c$ that gives the aggradation rate at an infinite distance from the channel belt, $d_c$ is the distance (m) to the nearest channel-belt cell and $b$ is the floodplain aggradation exponent (m). Equation 14 is similar to that of Mackey & Bridge (1995) and Törnqvist & Bridge (2002) and describes the commonly observed exponentially decreasing floodplain aggradation rate with increasing distance from the channel belt. However, in Eq. 14, exponent $b$ is dimensional (the Mackey–Bridge exponent is dimensionless), and is the reciprocal of the floodplain aggradation exponent used by Mackey and Bridge. Furthermore, the introduction of $C$ (not in the Mackey–Bridge model) allows a finite-deposition rate at long distances from the channel belt. Downstream fining of sediment cannot be simulated in this model, because the grain-size of transported sediment is not described explicitly.

Hill slope degradation is simulated for the floodplain area simultaneously with aggradation, using a local drain direction network calculated for each time step. In the local drain direction network, each cell is assigned a single direction of the locus of maximum topographical slope calculated with the eight-point pour algorithm (Moore, 1996; Burrough & McDonnell, 1998). For a cell on this local drain direction network, hill slope degradation ($\lambda$, m year$^{-1}$) is calculated for each time step with the familiar transport limited erosion model (Prosser & Rustomji, 2000; Hancock *et al.*, 2002; Tucker & Whipple, 2002; Whipple & Tucker, 2002):

$$\lambda = \gamma q_h^{\alpha} s^{\beta} \quad (15)$$

in which $q_h$ is the surface run-off from the cell (m year$^{-1}$), $s$ is the slope of the cell and $\alpha$, $\beta$ and $\gamma$ are parameters. As $\alpha$ and $\beta$ are normally assumed to equal unity, parameter $\gamma$ is dimensionless. $q_h$ is calculated as the sum of all net precipitation ($P$, m year$^{-1}$) values of cells uphill of the cell under consideration, over the local drain direction network. The slope $s$ is calculated as the topographical gradient between the cell itself and its direct downhill neighbour over the local drain direction network. The net aggradation of a cell outside the channel belts equals $g$ (Eq. 14) minus $\lambda$.

During incision of a channel belt, leading to a channel-belt elevation below the adjacent floodplain, the cells on the edge of the channel belt receive sediment from the adjoining hill slopes, which is transported over the local drain direction network towards the channel belt. This sediment is added as input $i$ (Eq. 3) to the nearest arc of the channel network. The surface run-off ($q_h$) from the hill slope reaching the channel belt is not added to the channel network as discharge because, in these simulations, it is negligible compared with the amount of water ($Q_s$) that enters the channel network at the inflow point.

The model includes modules for compaction according to the approach followed by Mackey & Bridge (1995), but these are not used here because the thickness of the deposit in the scenarios presented is very thin. In addition, tectonic tilting and faulting are possible in the model but not used here. The model is written using PCRaster functions operating on 2D and 3D entities embedded in the Python programming language (cf. Karssenberg & De Jong, 2005; Karssenberg *et al.*, 2007).

## MODEL OUTPUTS

The model stores a set of variables as a time series of raster maps, representing the positions of channel belts, water and sediment discharge for each channel belt, and surface topography. In addition, the resulting alluvial architecture is stored in three dimensions, using voxels of variable thickness (Karssenberg & De Jong, 2005), resulting in an exact representation of the geometry of depositional layers in the vertical direction. In addition to these model outputs, the following variables and statistics are calculated by the model. A *bifurcation initiation* is the addition of a new bifurcation to the channel network. The *bifurcation initiation time* is $t$ (year) at the time step a bifurcation is created. The *bifurcation duration* (year) is $t$ (year) at the time step the bifurcation is removed minus the bifurcation initiation time. The *bifurcation frequency*

is the number of bifurcation initiations per year, calculated as the average over a time interval of 500 years. Some statistics are calculated for bifurcations of avulsion type only, excluding unsuccessful and removed inflow channel bifurcations, these are avulsion duration and avulsion frequency, calculated in the same way as bifurcation duration and frequency. The *number of channels on the floodplain* is the total number of channels at time $t$ on the floodplain.

The average aggradation rate (m year$^{-1}$) is calculated over a time window of 50 years. The total probability for a bifurcation given a high flood discharge ($P_{\mathrm{tot}}$) at a time step is:

$$\begin{aligned} &\text{for } i = 1 \text{ to } n\text{:} \\ &\qquad p_i = (1 - p_{i-1})P_i(B), \qquad (16) \\ &P_{\mathrm{tot}} = p_i \end{aligned}$$

in which $n$ is the number of cells at the edge of channel belts and $P_i(B)$ is the probability calculated from Eq. 10 for a cell $i$ at the edge of a channel belt. Note that $P_{\mathrm{tot}}$ is the total probability for a bifurcation *given* a high flood discharge (Eq. 10).

## ESTIMATING MODEL PARAMETERS

Although a detailed comparison of the model with real-world data is not the aim here, values of parameters and input variables (Table 1) are chosen to create a model run that approximately represents the Holocene Rhine–Meuse delta (Törnqvist, 1993, 1994; Stouthamer & Berendsen, 2000, 2001, 2007; Berendsen & Stouthamer, 2001; Makaske, 2001; Gouw & Berendsen, 2007). The values of $s_{\mathrm{f}}$ and $e$ (Table 1) result in a channel at the start of the model run with a slope of 0·0001. Under the assumption of zero aggradation or degradation when input variables, particularly base level ($H$, Eq. 4), sediment supply ($Q_{\mathrm{s}}$) and water supply ($Q_{\mathrm{w}}$), are kept constant, the parameter $a$ related to the diffusion of sediment through the streams is calculated by solving Eq. 2 for $a$ using values for $Q_{\mathrm{s}}$ and $Q_{\mathrm{w}}$ (Table 1) estimated to be representative of the Rhine–Meuse delta with the initial channel gradient $\partial h/\partial x_{\mathrm{c}}$ of 0·0001. The bank erodibility ($c$) is determined by a visual comparison between the width of channel belts in the Rhine–Meuse delta (Berendsen & Stouthamer, 2001; Cohen, 2003; Gouw & Erkens, 2007) and the width of those modelled. The parameters related to hill slope degradation (Eq. 15) are chosen from a visual interpretation of the geometry of the incised valley under base-level fall keeping parameter values in the order of magnitude of those given in the literature (Prosser & Rustomji, 2000; Hancock *et al.*, 2002; Tucker & Whipple, 2002; Whipple & Tucker, 2002). The floodplain aggradation exponent ($b$) is chosen based upon the values given by Bridge (1999), Mackey & Bridge (1995) and Törnqvist & Bridge (2002). The fraction $C$ is given a value of 0·2, such that the floodplain sedimentation rate at infinite distance from the channel belt is 0·2 $g_{\mathrm{c}}$. The Manning's $n$ roughness value of 0·04 (s m$^{-1/3}$) is representative of natural stream channels (Chow *et al.*, 1988). An amount of net precipitation ($P$) is used which occurs in temperate climates.

The parameters used to calculate the bifurcation probability ($\kappa$, $\mu$ in Eq. 10), and those related to discharge and stability of bifurcations ($\sigma^2$, $u_{\mathrm{crit}}$), are chosen such that the modelled avulsion frequency and the number of co-existing channels on the floodplain are in the order of magnitude of those observed in the Rhine–Meuse delta over the past 9000 years (Törnqvist, 1993; Berendsen & Stouthamer, 2001; Stouthamer & Berendsen, 2001; Gouw & Erkens, 2007). During this period, base level rose by about 20 m (Van de Plassche, 1995; Cohen, 2005), avulsion frequency was 0·009 year$^{-1}$, the number of co-existing channels was two to five (Stouthamer & Berendsen, 2001). The set of parameter values used can be considered to be realistic, but not unique. The sensitivity of the model to changes in parameter values is discussed at the end of the paper.

## EFFECTS OF EXTRINSIC FACTORS ON SYSTEM BEHAVIOUR AND ALLUVIAL ARCHITECTURE

Running the model and keeping the parameter values and input variables constant at the values given in Table 1 produces a fluvial system in dynamic equilibrium with negligible aggradation or degradation and no bifurcations. When input variables are changed, the fluvial system starts to evolve. This effect was studied for three scenarios whereby each scenario considers the sinuous change of a single input variable keeping all other input variables and parameters constant at values given in Table 1. The *base-level rise scenario* and the *base-level fall then rise scenario* use a change in base level ($H$, m) of 10 m over 10 000 years. In the *sediment supply scenario,* the channel-belt sediment supply quadruples over 10 000 years. The scenarios are discussed in detail below. Although model parameters have

**Table 1.** Nomenclature.

| | | |
|---|---|---|
| $a$ | 0·0127 | Parameter in slope-dependent sediment transport equation |
| $\alpha$ | 0·2 | Parameter in hill slope degradation equation |
| $b$ | 2000 | Floodplain aggradation exponent (m) |
| $\beta$ | 1·5 | Parameter in hill slope degradation equation |
| $c_l$ | 200 | Cell length (m) |
| $c$ | 0·0003 | The bank erodibility (year$^{-1}$) |
| $C$ | 0·2 | Sedimentation rate at infinite distance from the channel belt |
| $d$ | | Flow depth (m) at a specific arc |
| $d_c$ | | Distance (m) to nearest channel-belt cell |
| $D$ | | The event (FALSE or TRUE) of a yearly flood discharge possibly leading to a bifurcation |
| $e$ | 0·02 | Upper bound of uniform distribution used for noise term in initial topography (m) |
| $g$ | | Overbank aggradation rate (m year$^{-1}$) |
| $g_c$ | | Aggradation rate (m year$^{-1}$) at nearest channel belt |
| $\gamma$ | 14 | Parameter in hill slope degradation equation |
| $h$ | | Land surface elevation (m) |
| $H$ | | Base level (m) |
| $i$ | | Sediment input from hill slopes to an arc (m$^2$ year$^{-1}$) |
| $j$ | $32 \times 10^6$ | Conversion constant m$^3$ year$^{-1}$ to m$^3$ sec$^{-1}$ |
| $\kappa$ | 0·055 | Slope ratio proportionality constant |
| $l$ | $6 \times 10^4$ | Down-valley length of modelling area (m) |
| $\lambda$ | | Hill slope degradation (m year$^{-1}$) |
| $m$ | | Maximum channel-belt width (m) of an arc |
| $\mu$ | 5 | Slope ratio exponent |
| $n$ | 0·04 | Manning's $n$ (s m$^{-1/3}$) |
| $P$ | 0·5 | Net precipitation (m year$^{-1}$) |
| $P(B)$ | | Probability of a bifurcation given a high flood discharge |
| $P(D)$ | | Probability of a yearly flood discharge possibly leading to a bifurcation |
| $P_{tot}$ | | Total probability of a bifurcation given a high flood discharge |
| $q_0$ | | Water discharge (m year$^{-1}$) upstream of bifurcation |
| $q_i$ | | Water discharge (m year$^{-1}$) of a bifurcating channel $i$ |
| $q_h$ | | The surface run-off (m water slice spread over the cell per year) on hill slope |
| $q_s$ | | Sediment transport (m$^3$ year$^{-1}$) through a specific channel |
| $Q_s$ | $1 \times 10^6$ | Sediment supply (m$^3$ year$^{-1}$) at the inflow point |
| $q_w$ | | Water discharge (m$^3$ year$^{-1}$) through a specific channel |
| $Q_w$ | $7{\cdot}9 \times 10^{10}$ | Water discharge (m$^3$ year$^{-1}$) at inflow point |
| $r_s$ | | Slope ratio |
| $s$ | | Slope on hill slope |
| $s_f$ | 0·00011 | Initial slope of floodplain |
| $s_i$ | | Slope of a bifurcating channel $i$ directly downstream of bifurcation point |
| $s_{par}$ | | The slope in the direction parallel to the channel belt |
| $s_{per}$ | | The slope in the direction perpendicular away from the channel belt |
| $\sigma^2$ | 0·0036 | Variance of noise term in slope calculation of bifurcating streams |
| $t$ | | Time (year) |
| $t_{end}$ | 10 000 | Time at end of model run (year) |
| $t_{st}$ | 0 | Time at start of model run (year) |
| $\Delta t$ | 1 | Duration of one time step (year) |
| $u(0,e)$ | | Uniform noise term (m) for initial floodplain topography |
| $u_i$ | | Discharge ratio of bifurcating channel $i$ |
| $u_{crit}$ | 0·4 | Critical discharge ratio |
| $w$ | $2 \times 10^4$ | Cross-valley width of modelling area (m) |
| $w_c$ | | Width (m) of the channel at a specific arc |
| $w_{cb}$ | | Width (m) of a channel belt at a specific arc |
| $x$ | | Cell centre x coordinate (m), origin at bottom left corner |
| $x_c$ | | Downstream distance along a channel (m) |
| $y$ | | Cell centre y coordinate (m), origin at bottom left corner |
| $z$ | 1·0 | Channel side slope |

The second column provides values of parameters and input variables used for the base scenarios. Note that $Q_s$ is constant for all runs except the scenario with increasing sediment input, $t_{end}$ is 20 000 for the scenario with base-level fall and rise.

 

been selected to resemble the Holocene Rhine–Meuse delta, close comparison between the model and this real-world example is not attempted because many extrinsic factors, such as base-level change, sediment supply, water supply and tectonism, were not varied simultaneously in the model, as happened in the Rhine–Meuse delta during the Holocene (Stouthamer & Berendsen, 2000, 2001, 2007; Cohen, 2003, 2005). The scenarios in the present study aim to describe the effects of single extrinsic factors.

## Effect of base-level rise on floodplain dynamics and alluvial architecture

The base-level rise scenario (Figs 2 to 5, Animation S1 in *Supplementary material*) had aggradation in the whole modelling area. Although aggradation started downstream, average aggradation rates became approximately equal upstream and downstream after $t = 1 \times 10^3$ years, as a result of a fast upstream migration of a wave of aggradation to the upstream part of the modelling area at the start of the model run. The total aggradation at the end of the model run was everywhere approximately equal to total base-level rise (10 m), apart from a larger amount of aggradation close to the inflow point as can be seen in Fig. 5. A network of channels and channel belts was almost continuously changing due to bifurcations and avulsions. As can be seen in Fig. 3, new channels followed the steepest downstream path over the floodplain topography at the moment of bifurcation. For each channel, channel-belt width increased through time resulting in channel belts of various widths (Figs 3 to 5).

The total probability of bifurcations and the frequency of bifurcations and avulsions (and hence the number of co-existing channel belts on the floodplain) increased with the floodplain slope ratio, which increased with aggradation rate. During the initial 1000 to 2000 years of low rate of sea-level rise, when aggradation rate was low and decreased up-valley, a few bifurcations occurred down-valley (Fig. 2B and C). After about 2000 years, bifurcations and avulsions started to occur along the whole length of the floodplain (Figs 2B, C and 3), in response to average aggradation rates that did not vary along the floodplain length. After about 2000 years, the results did not show a marked relationship between the rate of base-level rise and bifurcation frequency. Instead, variation occurred in bifurcation frequency and number of co-existing channel belts over periods of between $0{\cdot}5 \times 10^3$ and $2 \times 10^3$ years (Fig. 2D and F). In addition, there were similar shorter-period variations in average aggradation rate (Fig. 2G). This variation has a random character because other realizations of the same scenario show different patterns during aggradation, as shown in the example of Fig. 6. The random character of this variation and the short period of the variation compared with the period of the base-level change ($2 \times 10^4$ years) indicate that it is caused by intrinsic system dynamics (i.e. it is autogenic) as will be discussed in the next section.

The avulsion frequency of the Holocene Rhine–Meuse delta also shows variation with periods of hundreds of years to about a thousand years (Stouthamer & Berendsen, 2001) and the avulsion frequency is in the same order of magnitude as modelled here, although it should be noted that model parameters have been adjusted until a comparable average avulsion frequency occurred as found in the Rhine–Meuse delta. Avulsions also move upstream at the start of base-level rise and after that occur along the whole length of the floodplain of the Rhine–Meuse delta, as they do in the model. The increasing number of coexisting channels with increasing frequency of bifurcations, as observed in the model results, was recognized in the Rhine–Meuse delta by Stouthamer & Berendsen (2001) and is probably also associated with an increased degree of anastomosing (Törnqvist, 1994). In the Rhine–Meuse delta, different channels can coexist for centuries, as simulated in the model.

The width of channel-belt deposits ranges between 200 and 4000 m (e.g. Fig. 4), and the variation in width ($w_{cb}$ at the moment of abandonment) between different channel-belt deposits is relatively large compared with the variation in width along an individual channel belt (with a constant duration of existence). The variation in width between different channel belts is a function of differences in channel gradient ($s_c$), water discharge ($q_w$) and duration of existence of a channel belt (Eqs 6, 7 and 9). Table 2 shows that the contribution of variation in channel gradient ($s_c$) to variation of the maximum channel-belt width ($m$) is small compared with the contribution of variation in water discharge ($q_w$) to the variation in $m$. In addition, only a small fraction of channel-belt deposits reached a channel-belt width ($w_{cb}$) that is close to the maximum width $m$, such that most channel belts were still increasing in width when they were abandoned. Therefore, it can be concluded that differences in width between channel belts are mainly caused by differences in discharge and duration of

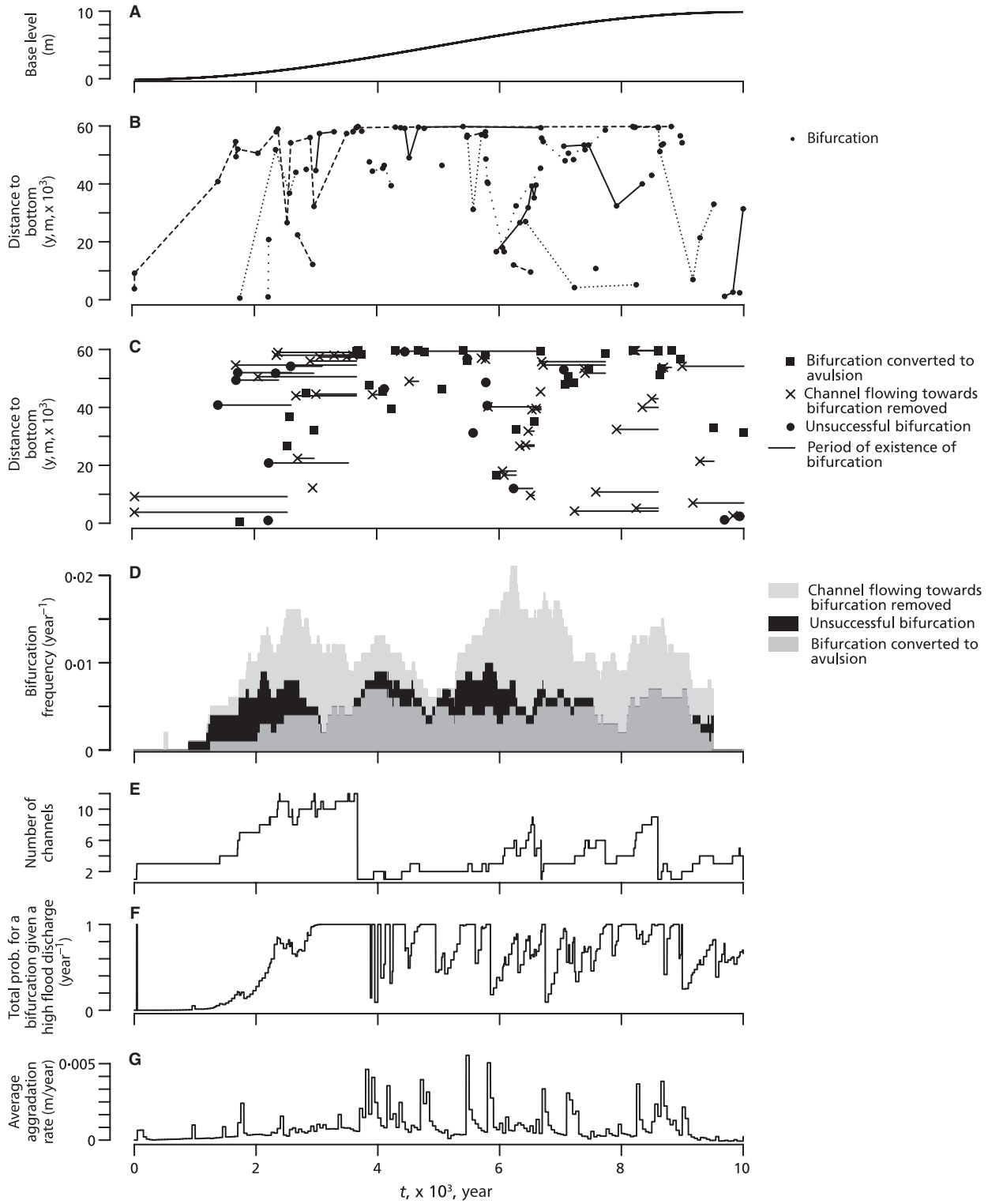


**Fig. 2.** Base-level rise scenario, base realization. The horizontal axis is time, $t$ (kyr). (A) $H$, base level (m). (B) The location of bifurcation initiations (dots) is given as the distance away from the bottom of the modelling area. Bifurcation initiations along the same channel belt are connected by a dashed line. (C) The location of bifurcation initiations is given as the distance away from the bottom of the modelling area (dots, squares and crosses). Horizontal lines represent the period of existence of each bifurcation. (D) Floodplain-averaged bifurcation frequency calculated over a moving window of 500 years. (E) Number of channels on the floodplain. (F) $P_{tot}$, the total probability for a bifurcation given a high flood discharge (Eq. 16). (G) Floodplain-averaged aggradation rate (m year$^{-1}$).

 

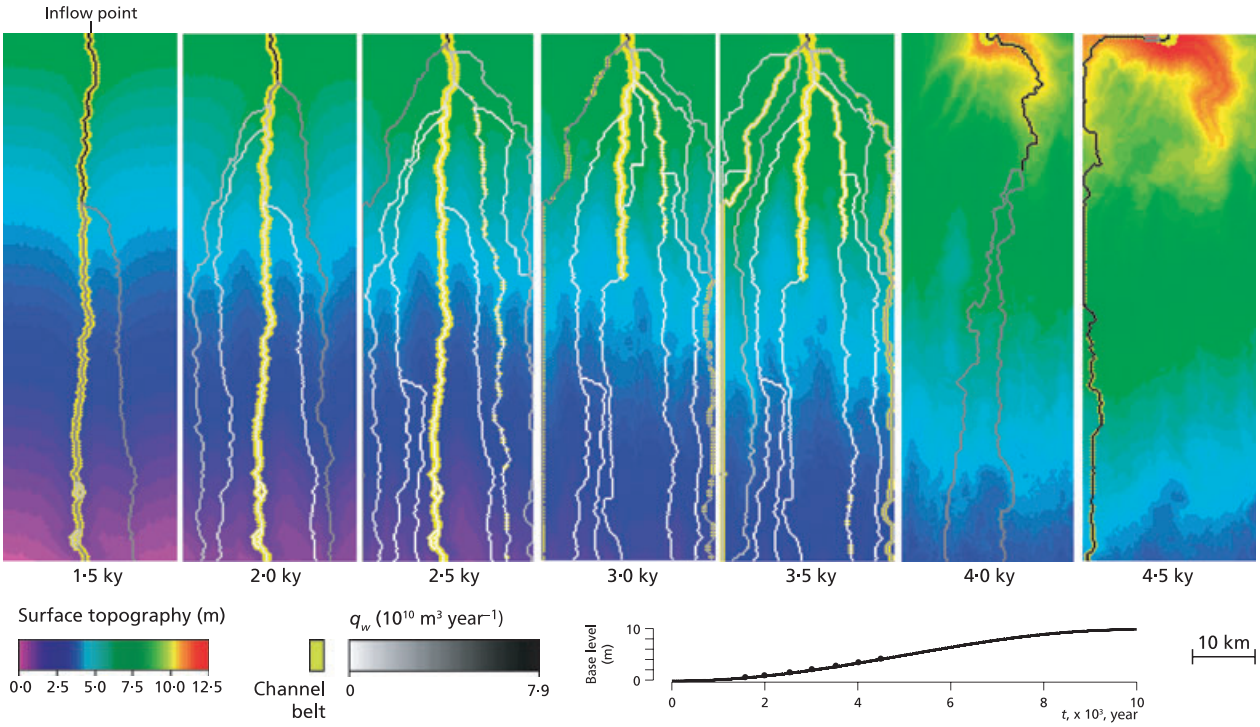


**Fig. 3.** Base-level rise scenario, base realization. Time series of water discharge ($q_w$, m$^3$ year$^{-1}$) for each channel belt, area of channel belts and surface topography ($h$, m). The base-level curve indicates the time slices shown.

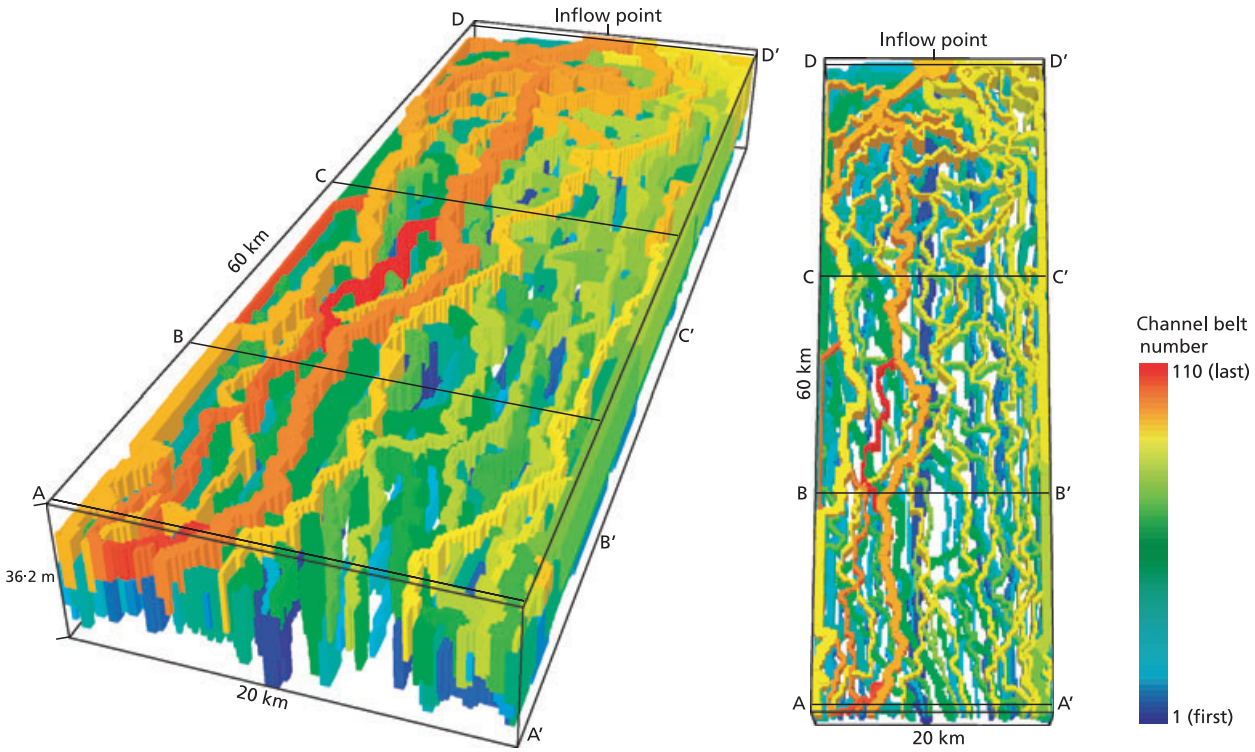


**Fig. 4.** Base-level rise scenario, base realization. Individual channel belts, perspective views.

existence, whereas differences in channel gradient play a minor role. The pattern of wider channel belts upstream and narrower channel belts downstream (Figs 4 and 5) is caused mainly by the fact that channels upstream generally have a larger discharge and a longer duration of

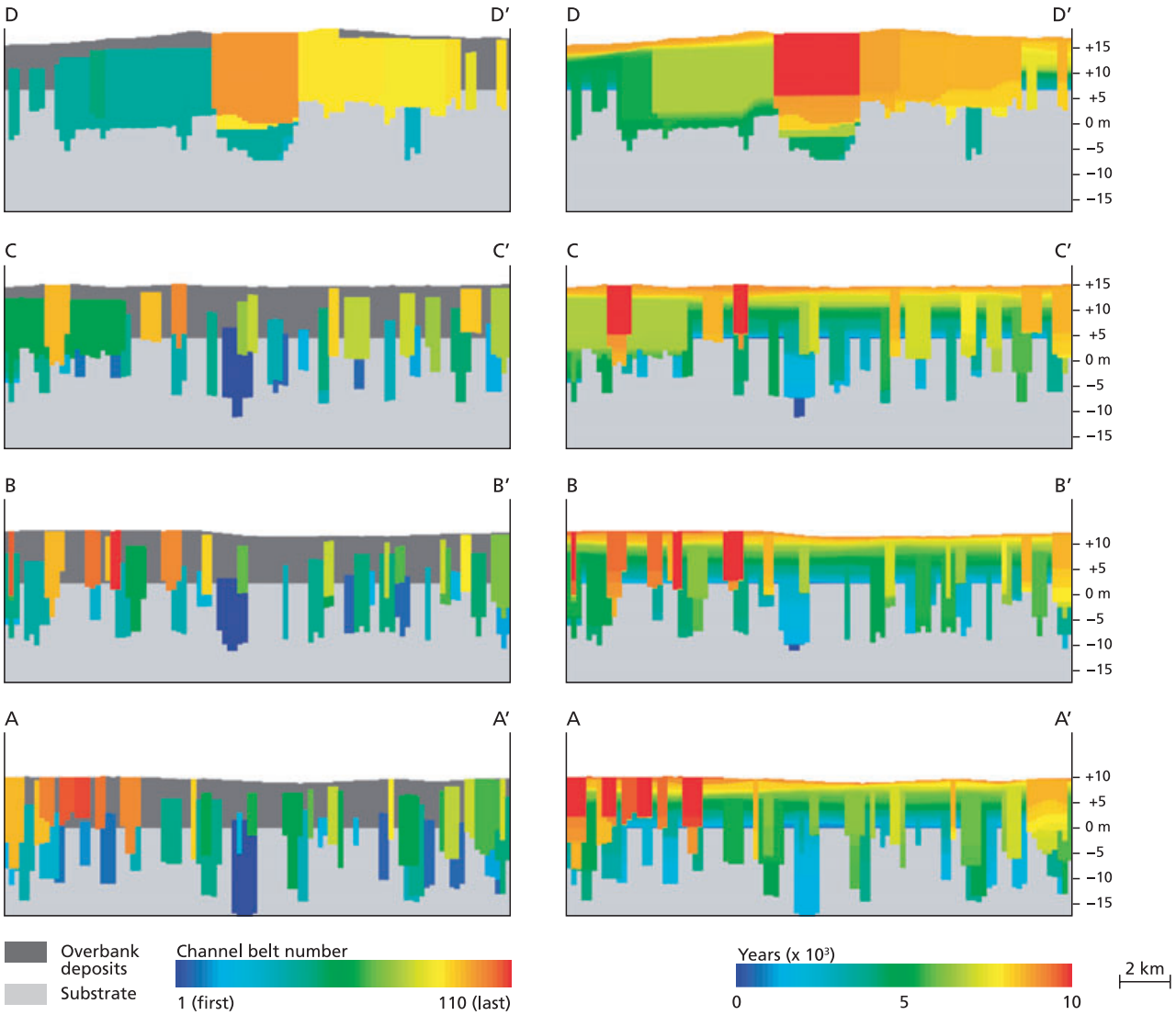


**Fig. 5.** Base-level rise scenario, base realization. Cross-sections at locations indicated in Fig. 4. Left: individual channel belts. Right: time (*t*, years) of deposition.

existence than channels downstream. The effect of a decrease in channel gradient in the downstream direction, which occurs for most of the time during base-level rise, is small compared with these effects. A downstream decrease in channel-belt widths can also be due to the nature of bank materials (Gouw & Berendsen, 2007; Makaske *et al.*, 2007), but this effect is not simulated with the current model. The variation in the channel-belt thickness is caused by variation in flow depth (*d*, Table 2) and differences in total aggradation over the period of existence of a channel belt.

Wide, connected channel belts are concentrated around the inflow point (Figs 4 and 5), because they are long-lived and fixed in position; this produces a high channel-deposit proportion. Narrower, and less connected, channel belts occur downstream, giving a lower channel-deposit proportion. As a result of the decrease in overbank aggradation away from channel belts, overbank aggradation and topography are relatively low at the floodplain margins; this results in a preferential clustering of channel belts at the margins. This clustering at the margins is particularly clear in Fig. 5, transect A–A′. Such channel-belt clustering was also simulated by Bridge & Leeder (1979) and Mackey & Bridge (1995).

## Effect of base-level fall then rise on floodplain dynamics and alluvial architecture

The falling base level in the base-level fall then rise scenario (Figs 7 to 10, Animation S2 in

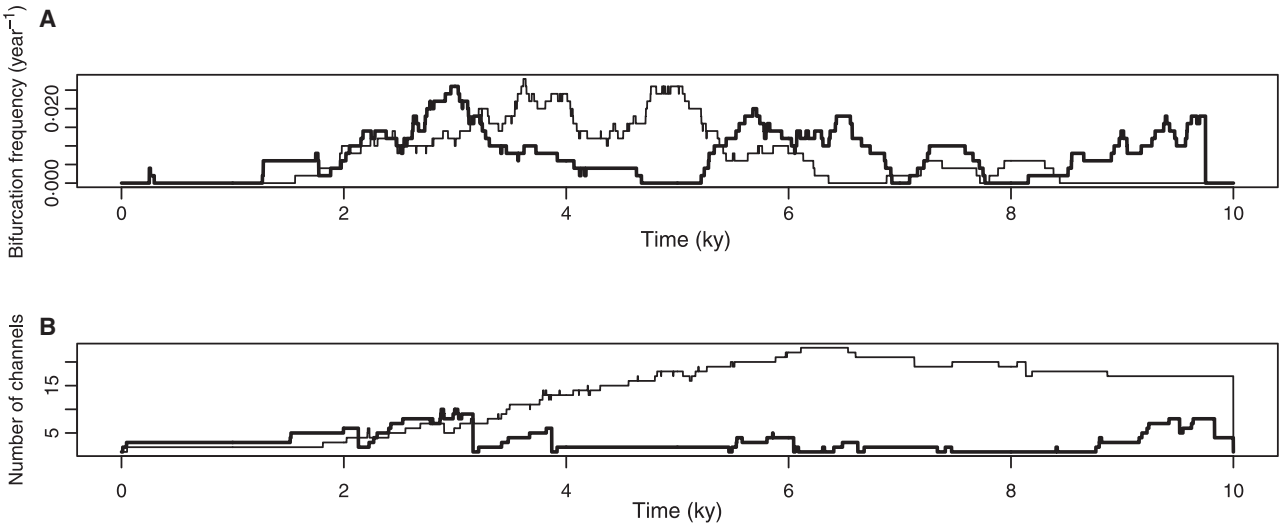


**Fig. 6.** Base-level rise scenario, two other realizations (represented by thin and thick lines). Horizontal axis is time, $t$ (years). (A) Bifurcation frequency calculated over a moving window of 500 years. (B) Number of channels on the floodplain.

*Supplementary material*) caused erosion and development of an incised valley which was deepest and widest at the downstream part of the modelling area (Fig. 8, $t = 1{\cdot}3 \times 10^3$ years). This incised valley contained a single channel belt that increased in width up to close to its maximum width ($m$, Eq. 7, Fig. 8). During base-level rise, aggradation occurred, starting in the downstream area, and the incised valley was completely filled up with channel belts and overbank deposits (e.g. Fig. 10). Bifurcation locations were initially down-valley where aggradation began, but they gradually moved upstream (Figs 7B, C and 8). Bifurcation frequency and aggradation showed short-period variations (Fig. 7D and G), as in the case for the previous sea-level rise scenario.

The upstream part of the floodplain contained multiple, superimposed channel belts that were wide and thick, due to the fixed location of the inflow point and the incision of the valley during falling sea-level (Fig. 10). Here, a few narrow channel belts occurred near the floodplain margins. Most of the floodplain contained a wide and thick, central channel belt near the base, which represented the incised valley fill. This valley fill was bordered and cut into by much narrower and thinner channel belts that formed during rising sea-level (Figs 9 and 10). The most recent channel belts were more numerous, narrower and thinner than the older ones. Channel belts were not concentrated near floodplain margins, as in the previous sea-level rise scenario.

Field and experimental studies and numerical modelling (Blum & Törnqvist, 2000; van Heijst & Postma, 2001; Swenson & Muto, 2007) indicate that aggradation can be going on upstream of floodplains, while degradation associated with sea-level fall is going on nearer the coast. This effect did not happen in this model scenario because the only variable extrinsic parameter was base level. However, upstream aggradation would have occurred in this model scenario if upstream sediment supply was increased simultaneously with base-level fall (see below).

The sequence stratigraphy models of Shanley & McCabe (1993) and Wright & Marriott (1993) show an incised valley bounded by river terraces, and filled with 'amalgamated' channel deposits, produced during base-level fall and early sea-level rise. These deposits are overlain by a wider sequence produced in the mid to late stages of sea-level rise containing individual channel

**Table 2.** Flow depth ($d$, m) and maximum channel-belt width ($m$, m) for different combinations of topographical slope ($s_c$) and discharge ($q_w$, m$^3$ year$^{-1}$) of the channel as calculated from Eqs 6 and 7. The values of $s_c$ and $q_w$ represent the range of values occurring in the scenarios.

| | $s_c$ | | | |
|---|---|---|---|---|
| | 0·00005 | | 0·0002 | |
| $q_w$ | $d$ | $m$ | $d$ | $m$ |
| $7{\cdot}9 \times 10^{10}$ | 14 | $6{\cdot}5 \times 10^3$ | 11 | $4{\cdot}3 \times 10^3$ |
| $0{\cdot}79 \times 10^{10}$ | 6 | $1{\cdot}7 \times 10^3$ | 5 | $1{\cdot}1 \times 10^3$ |

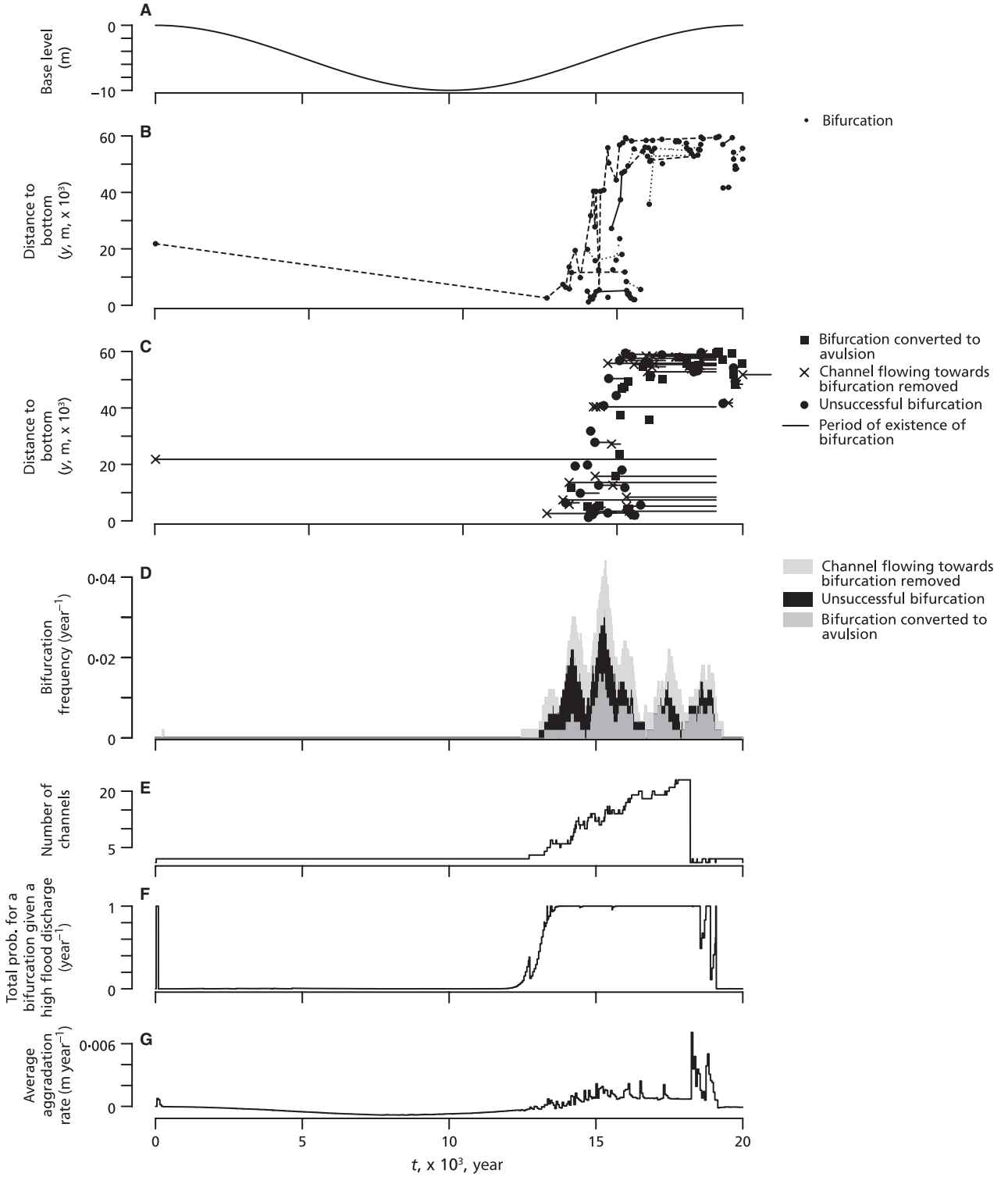


**Fig. 7.** Base-level fall–rise scenario, base realization. Horizontal axis is time, $t$ (kyr). (A) $H$, base level (m). (B) The location of bifurcation initiations (dots) is given as the distance away from the bottom of the modelling area. Bifurcation initiations along the same channel belt are connected by a dashed line. (C) The location of bifurcation initiations is given as the distance away from the bottom of the modelling area (dots, squares and crosses). Horizontal lines represent period of existence of each bifurcation. (D) Floodplain-averaged bifurcation frequency calculated over a moving window of 500 years. (E) Number of channels on the floodplain. (F) $P_{tot}$, the total probability for a bifurcation given a high flood discharge (Eq. 16). (G) Floodplain-averaged aggradation rate (m year$^{-1}$).

 

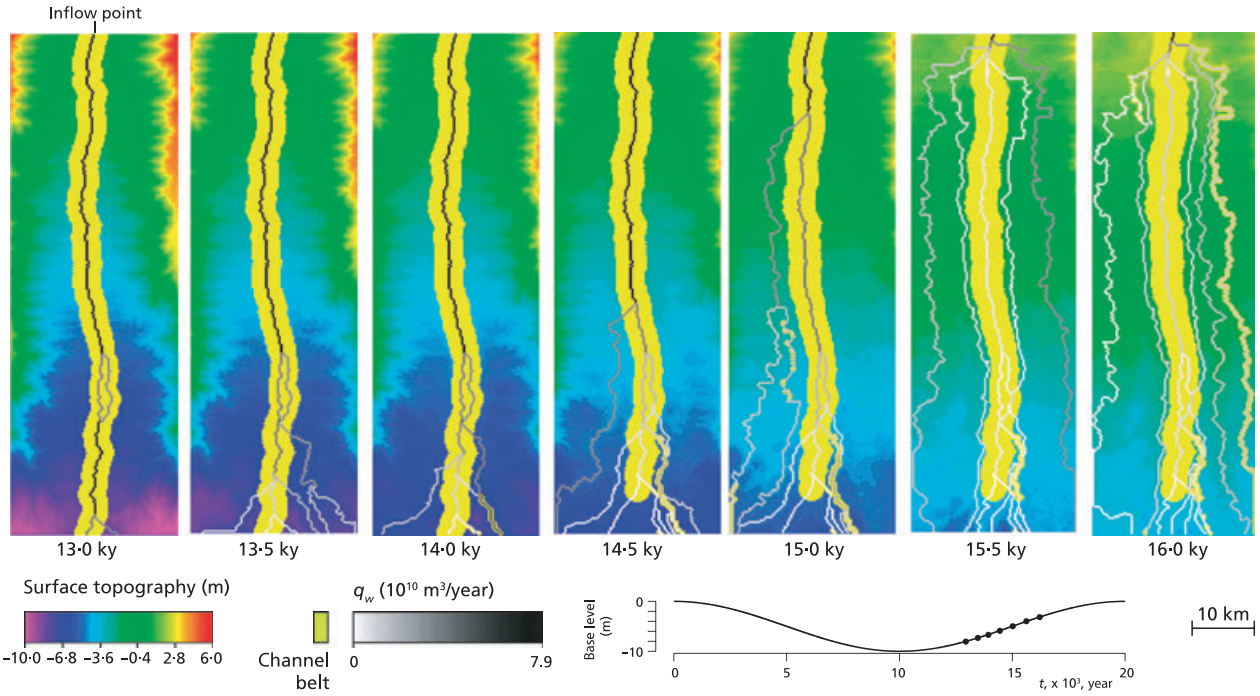


**Fig. 8.** Base-level fall–rise scenario, base realization. Time series of water discharge ($q_w$, $m^3$ $year^{-1}$) for each channel belt, area of channel belts and surface topography ($h$, m). Base-level curve indicates the time slices shown.

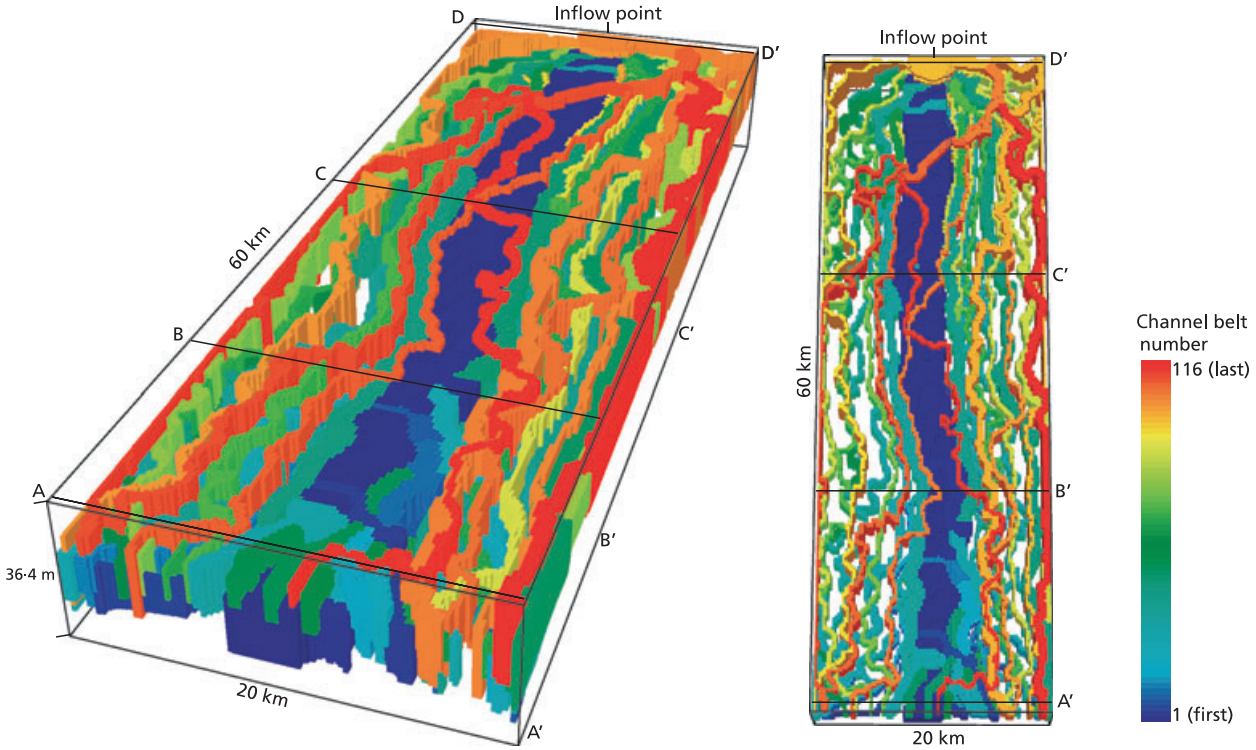


**Fig. 9.** Base-level fall–rise scenario, base realization. Individual channel belts, perspective views.

deposits encased in floodplain deposits, with a low channel-deposit proportion. The model results of the present study show considerable along-valley variation in alluvial architecture and substantial overlap of incised valley-fill deposits by deposits formed during sea-level rise. These

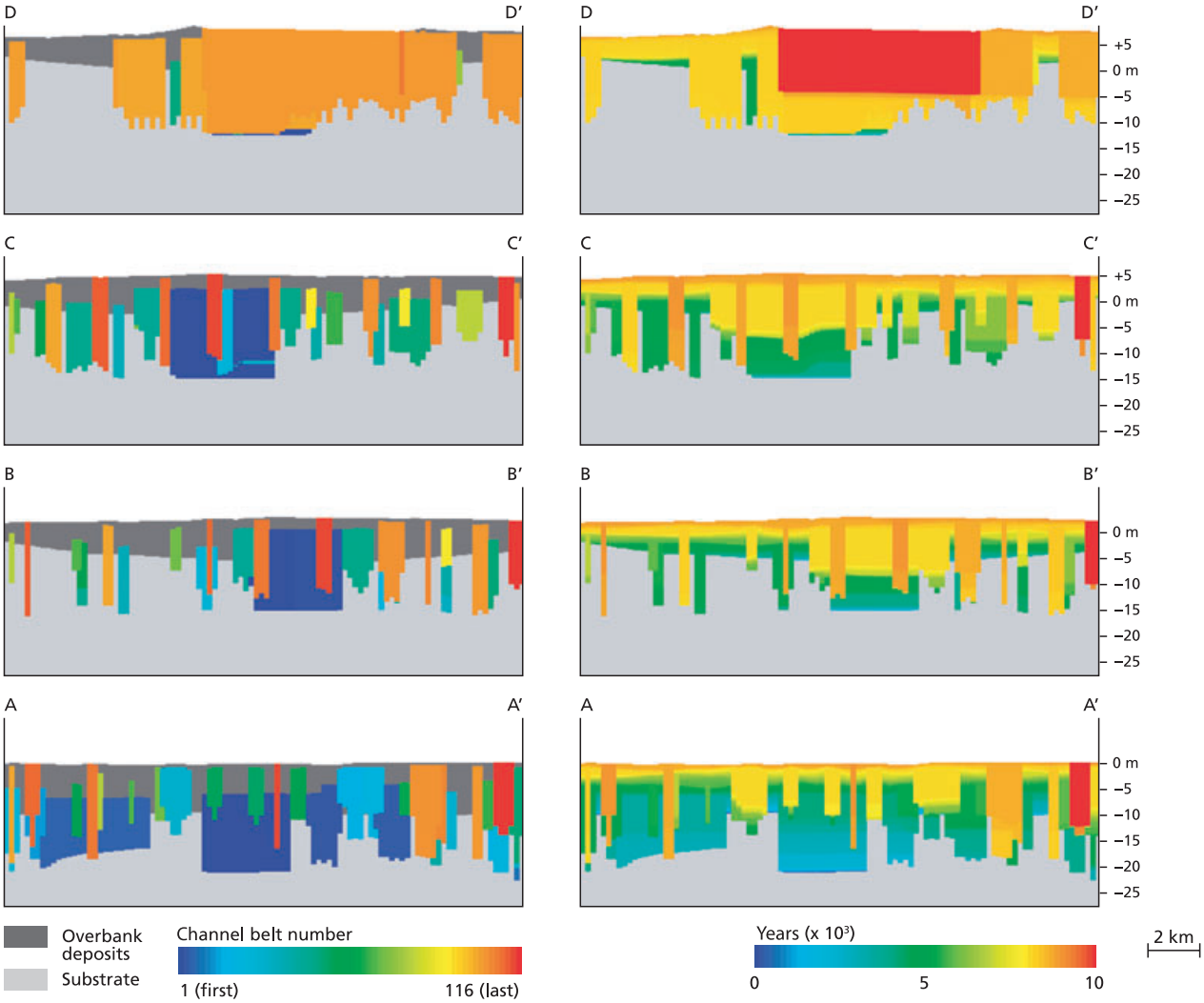


**Fig. 10.** Base-level fall–rise scenario, base realization. Cross-sections at locations indicated in Fig. 9. Left: individual channel belts. Right: time (*t*, years) of deposition.

results differ substantially from the sequence stratigraphy models. However, further analysis is desirable because model results do not include net aggradation associated with increases in sediment supply upstream.

## Effect of increasing sediment supply on floodplain dynamics and alluvial architecture

The sediment supply scenario (Figs 11 to 14, Animation S3 in *Supplementary material*) has an increasing sediment supply, as shown in Fig. 11A, starting with a value that would result in an equilibrium system (without net aggradation or degradation) under the given floodplain slope and water input. As a result of the increased sediment supply, the system increased its channel gradient resulting in aggradation upstream, while net aggradation downstream was zero due to the constant base level (Figs 12 and 14). As a result, an alluvial fan developed which increased in size through time, covering the upper part of the area at the end of the model run (Figs 12 and 13). A nodal avulsion site developed at the upstream inlet that produced a radial pattern of channel belts. The area downstream was less affected by the development of the fan, and the radial pattern in channel belts changed downstream to a pattern of approximately parallel channel belts.

Almost all bifurcations and avulsions occurred at the apex of the fan due to the highest aggradation rate in this area (Fig. 11B). The bifurcation frequency, number of coexisting channel belts and aggradation rate varied periodically with periods of hundreds of years (Fig. 11D, E and G),

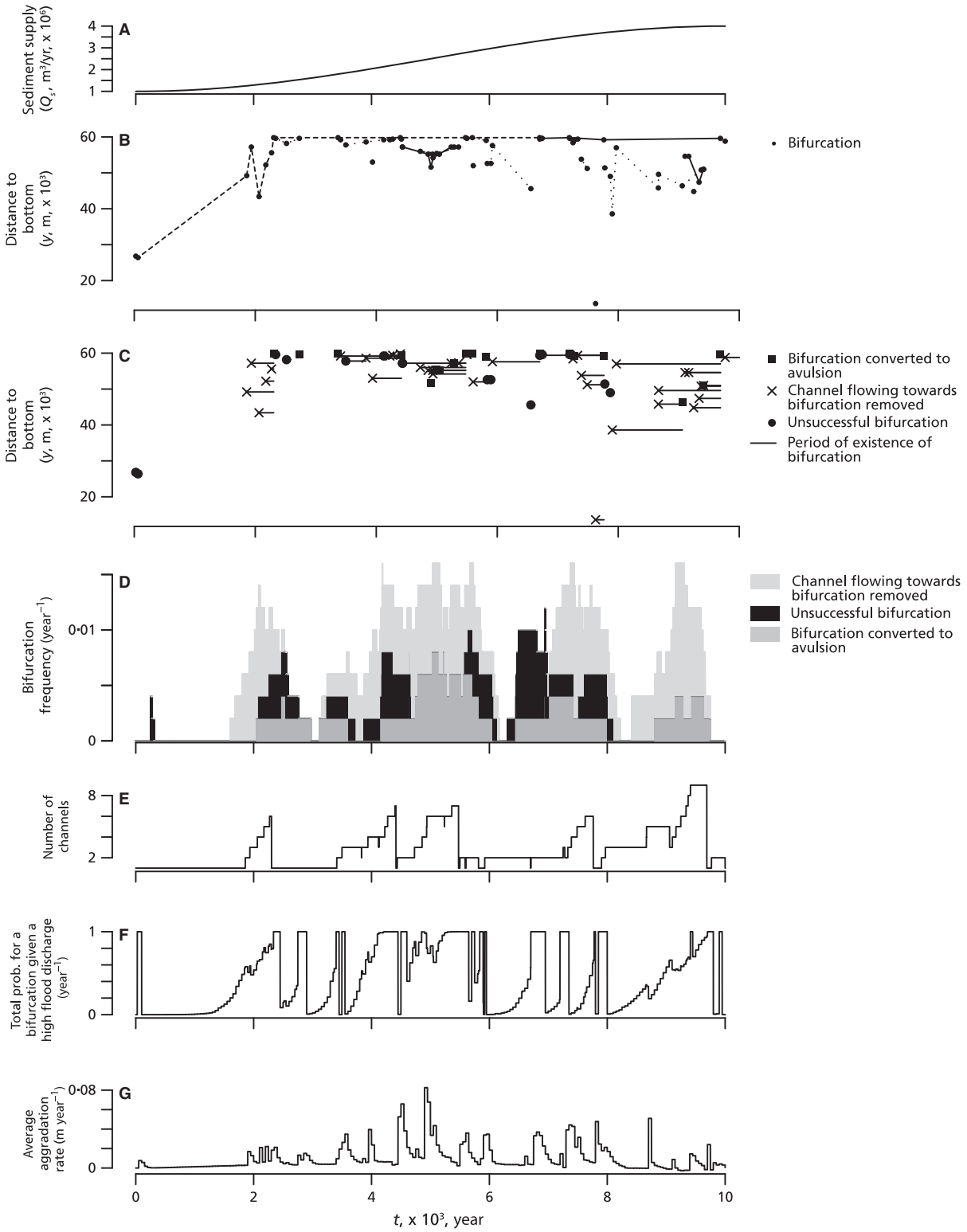


**Fig. 11.** Sediment supply scenario, base realization. Horizontal axis is time, $t$ (kyr). (A) $Q_s$, sediment supply ($m^3$ $year^{-1}$). (B) The location of bifurcation initiations (dots) is given as the distance away from the bottom of the modelling area. Bifurcation initiations along the same channel belt are connected by a dashed line. (C) The location of bifurcation initiations is given as the distance away from the bottom of the modelling area (dots, squares and crosses). Horizontal lines represent period of existence of each bifurcation. (D) Floodplain-averaged bifurcation frequency calculated over a moving window of 500 years. (E) Number of channels on the floodplain. (F) $P_{tot}$, the total probability for a bifurcation given a high flood discharge (Eq. 16). (G) Floodplain-averaged aggradation rate (m $year^{-1}$).

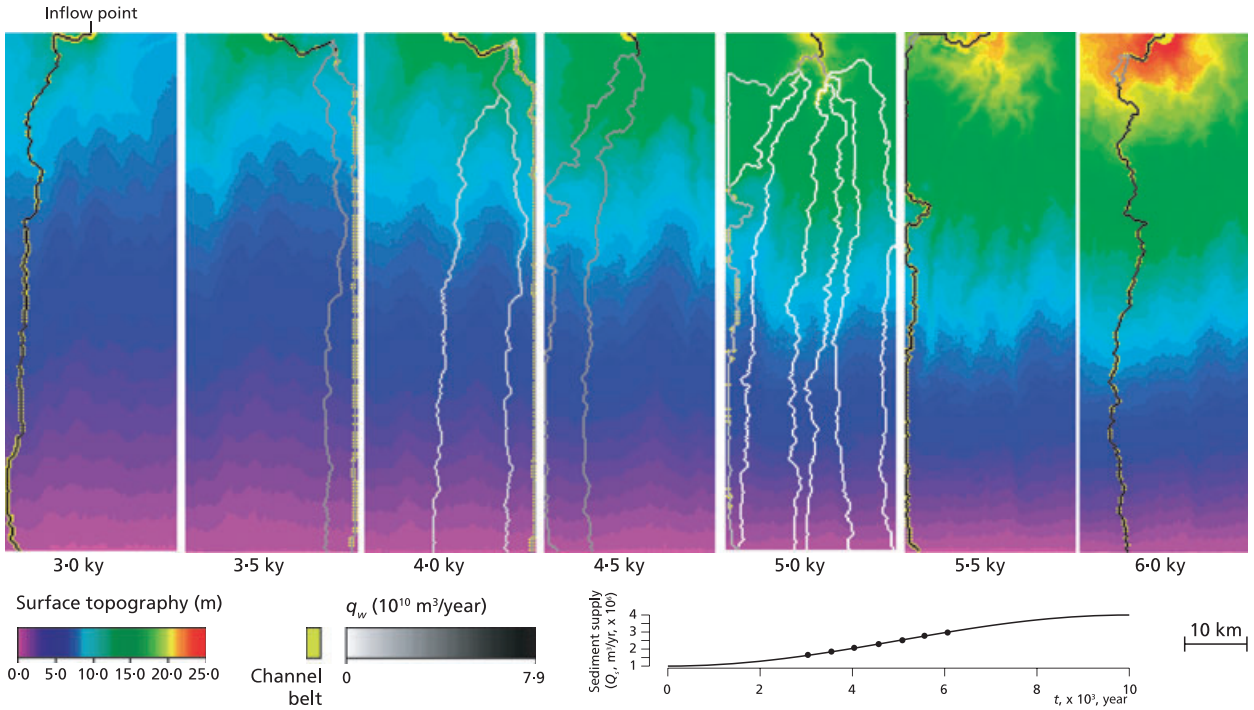


**Fig. 12.** Sediment supply scenario, base realization. Time series of water discharge ($q_w$, $m^3$ $year^{-1}$) for each channel belt, area of channel belts and surface topography ($h$, m). Sediment supply curve indicates time slices shown.

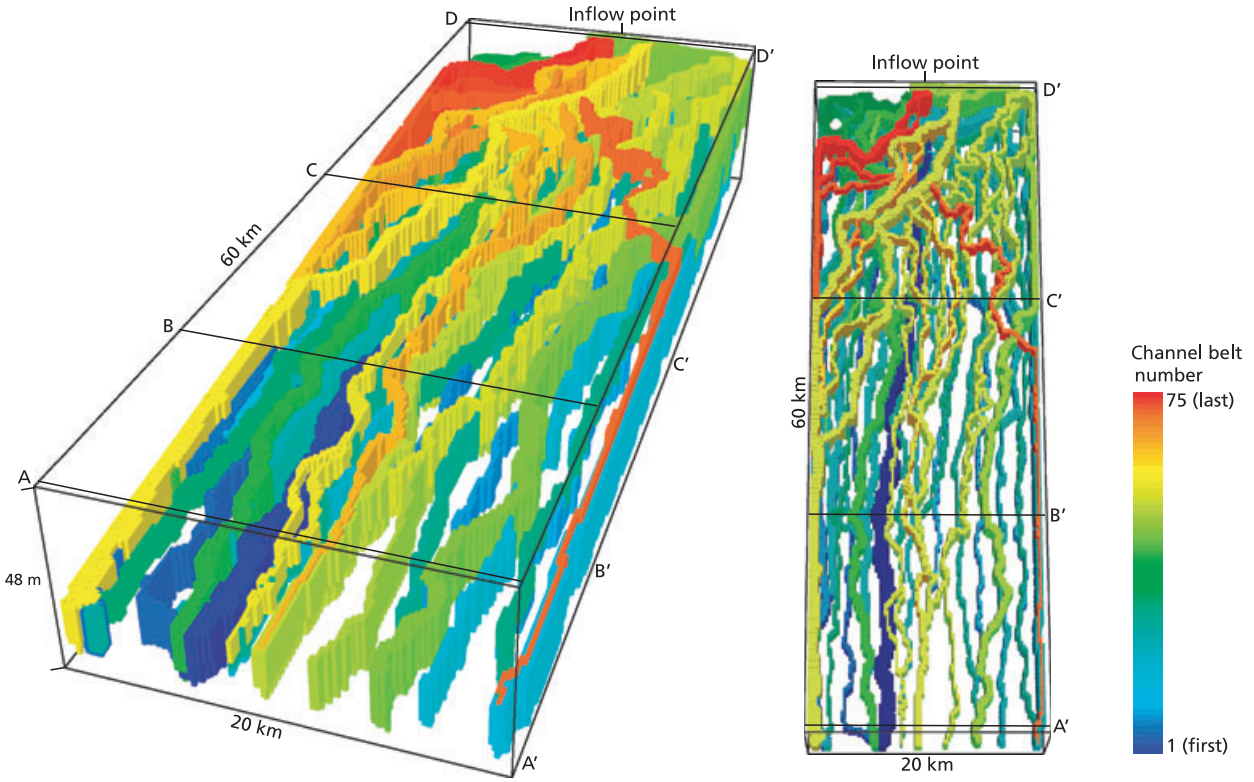


**Fig. 13.** Base-level fall–rise scenario, base realization. Individual channel belts, perspective views.

in a way similar to the base-level rise scenario. The periods of high aggradation rate generally coincided with periods of high bifurcation frequency, but the aggradation rate periods were shorter in duration. Fan-head entrenchment following avulsion, and deposition of a sediment

 

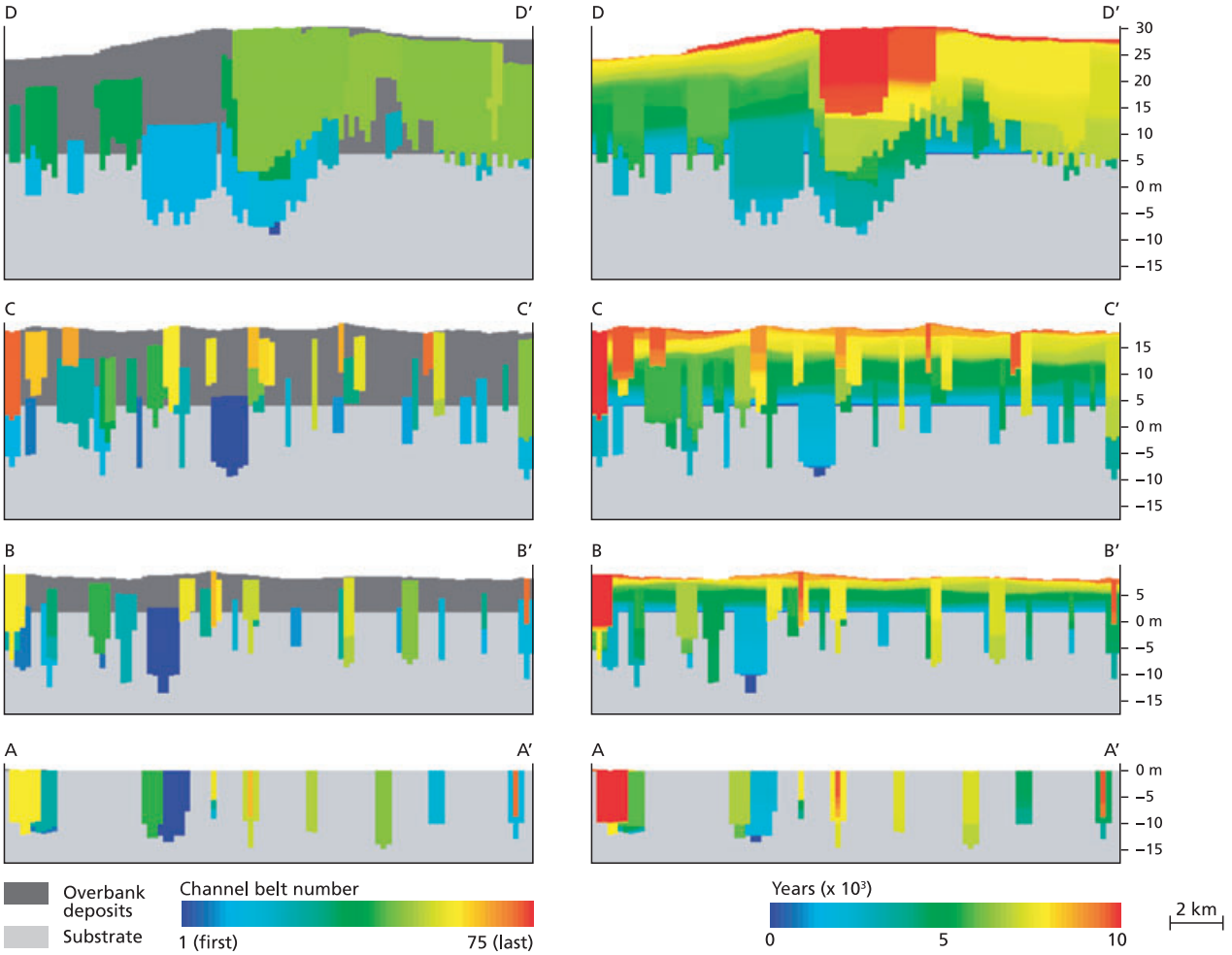


**Fig. 14.** Base-level fall–rise scenario, base realization. Cross-sections at locations indicated in Fig. 9. Left: individual channel belts. Right: time (*t*, years) of deposition.

lobe associated with the new channel (as described for experimental alluvial fans by Schumm *et al.*, 1987), were simulated by the model.

Near the fan apex, the channel belts were widest and thickest (Figs 13 and 14), due to the longevity and discharge of the channels. These channel belts were located near the inflow point (fan apex) and were, therefore, connected and formed a zone of high channel-deposit proportion. In this location, some smaller channel belts occurred at the margin of the fan apex. The width and thickness of channel belts decreased downstream, due to reduced discharge, longevity and aggradation rate.

The geometry of the alluvial fan produced by the model, the spatial distribution of channel belts, and the alluvial architecture is qualitatively comparable with modern, fluvial-dominated alluvial fans, and specifically the Kosi fan as described by Wells & Dorr (1987), Singh *et al.* (1993) and simulated by Mackey & Bridge (1995). However, the model did not simulate the progressive movement of channel belts in one direction across the fan, as happened in the Kosi fan.

## EFFECTS OF INTRINSIC FACTORS ON SYSTEM BEHAVIOUR AND ALLUVIAL ARCHITECTURE

Although changes in extrinsic factors (sediment supply and base level) over a period of 10 000 years or more controlled variation in aggradation rate, bifurcation frequency and bifurcation location at these timescales, variation in these output variables over shorter timescales (hundreds to 2000 years) cannot be explained by variation in extrinsic factors. This shorter-term variation was due to intrinsic factors related to inter-related processes and feedback within the

complex channel network. Two intrinsic processes are most important, as discussed below: (i) aggradation and degradation around new bifurcation points; and (ii) processes at bifurcation points that determine the duration and type of bifurcation.

### Aggradation and degradation around new bifurcation points

Figure 15 shows the effect of aggradation and degradation around a new bifurcation point. At the bifurcation initiation time, the new channel flowed into the overbank area with a relatively low topography. As a result, the new channel had a high slope ($s_c$) compared with that of the main channel. Two processes occurred in response to this high slope. Firstly, the old channel belt showed a period of degradation which extended upstream and downstream from the bifurcation point. Although this degradation extended over almost the whole length of the floodplain, it was greatest around the bifurcation point (Fig. 15C); as a result of this, the old channel belt was incised in its own levée for a period of *ca* 50 years. Secondly, the new channel belt filled up the lower overbank area, forming an elevated channel belt in this area (compare the topography on Fig. 15A with that on Fig. 15B). This process was associated with relatively high aggradation rates along most of the length of the new channel (Fig. 15D). Figure 15E shows the effect of these two processes on the total probability for a bifurcation given a high flood discharge ($P_{tot}$). Directly after the bifurcation initiation time, $P_{tot}$ fell due to the zero slope ratios ($r_s$) along the old, incised, channel belt. After *ca* 40 years, aggradation of the new channel belt resulted in increasing slope ratios there and $P_{tot}$ increased gradually.

An analysis of all bifurcations in the base-level rise scenario showed that the aggradation and degradation processes described above occurred for 90% of the bifurcations, and had at least three different effects on model behaviour. Firstly, the period between two consecutive bifurcation initiations was generally greater than several decades, due to the reduced probability of a new bifurcation occurring after a bifurcation. Secondly, after a bifurcation initiation at a certain location, the probability of occurrence of the next bifurcation was approximately equal for all of the channel reaches on the floodplain. Although the old channel belt potentially had higher slope ratios due to its longer period of aggradation compared with the new channel belt, slope ratios along the old channel belt were reduced for several decades as a result of incision of the old channel belt in its levées. After several decades, incision of the old channel belt changed to aggradation and slope ratios increased, but slope ratios also increased along the new channel belt due to the high aggradation rates there. As a result, the pattern of upstream shift of bifurcation points along individual channel belts, referred to as avulsion sequences by Mackey & Bridge (1995), did not occur. Figures 2B, 7B and 11B show that this pattern did not occur significantly more often compared with downstream shifts or random patterns. Mackey & Bridge (1995) over-estimated the slope ratios upstream of bifurcation points because their model was not capable of simulating the incision associated with bifurcation.

The third effect of a bifurcation was increased aggradation rate in the area containing the new channel belt and its associated floodplain deposits, as shown by the difference in topography on Fig. 15A and B. Although this was mainly a local effect, it had a major impact on the aggradation rate, as shown by the peaks in the aggradation rate, averaged over the whole floodplain (Figs 2G, 7G and 11G). An analysis of bifurcations and average aggradation rates for the base-level rise scenario showed that increased aggradation rate may occur for $2 \times 10^2$ years after the bifurcation initiation time. This process could be considered comparable with that which occurred in the Cumberland Marshes of Saskatchewan following an avulsion (Smith *et al.*, 1989, 1998). The high aggradation rate associated with the movement of the new channel into the adjacent flood basin produced frequent bifurcations, an anastomosing river system, and distinctive 'avulsion deposits'. Furthermore, this process may be analogous to the formation of depositional lobes on alluvial fans following avulsion (Schumm *et al.*, 1987).

### Processes at a bifurcation point determining bifurcation duration and type

An exploratory analysis of model outputs, including scatter plots of slope ratio against bifurcation duration for different model runs, showed that the slope ratio at the bifurcation point at the bifurcation initiation time affected the evolution of the bifurcation. A bifurcation initiated at a high slope ratio resulted in a new channel with a large gradient advantage over the old channel. As a result, the discharge ratio (Eq. 13) dropped within one to five years to a value below $u_{crit}$, and the

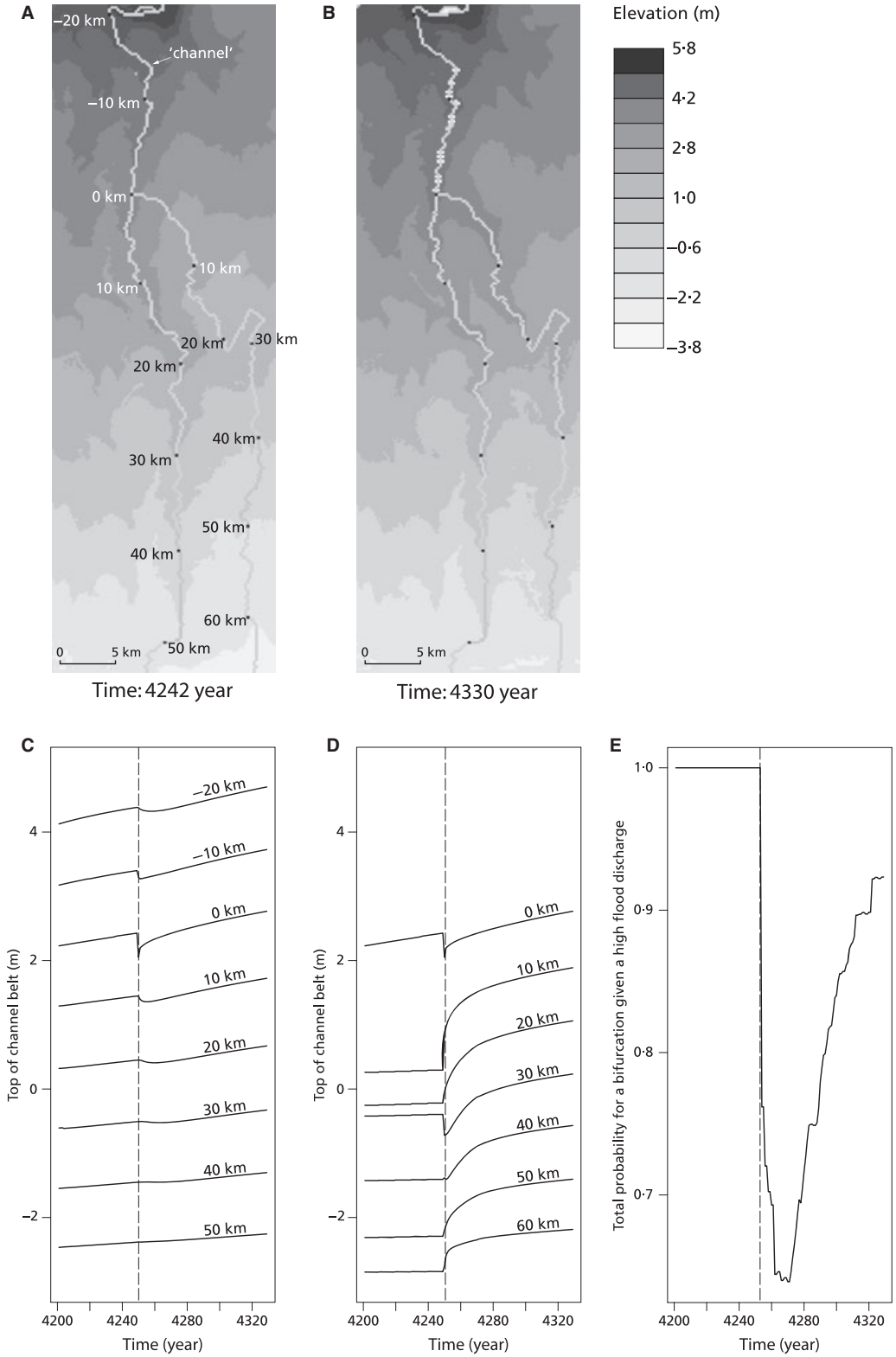


**Fig. 15.** Aggradation and degradation upstream and downstream of a bifurcation point. (A) Surface topography and channel belts directly after the bifurcation initiation time. Channel belt on the right-hand side of the figure is the new channel belt. (B) Surface topography and channel belts 88 years after the bifurcation. (C) Surface topography at positions along the old channel belt. (D) Surface topography at positions along the new channel belt. (E) $P_{tot}$, the total probability for a bifurcation given a high flood discharge (Eq. 16). Vertical dashed line in (C), (D) and (E) indicates the bifurcation initiation time.

bifurcation changed into an *avulsion*. Most of the bifurcations of type *avulsion* in Figs 2C, 7C and 11C were such instant avulsions with a short period of existence. However, bifurcations created at lower values of the slope ratio reached a situation with almost equal gradients ($s_1$ and $s_2$ in Eq. 12) for both bifurcating channels within a few decades. As a result, these bifurcations could remain stable for longer periods of time, as shown by the bifurcations with a longer period of existence in Figs 2C, 7C and 11C, because the critical discharge ratio ($u_{crit}$, described below; Eq. 13) was not reached. These bifurcations became a *removed inflow channel bifurcation* due to changes upstream, or changed into an *avulsion* or an *unsuccessful bifurcation* as a result of either: (i) new channels connecting close to the bifurcation point of existing channels, having effects on channel gradients at the bifurcation point; or (ii) local variations in channel gradient at the bifurcation point modelled using the noise terms $n_1$ and $n_2$ (Eq. 12). These processes may result in one of the two distributaries downstream of the bifurcation point becoming inactive (Eq. 13).

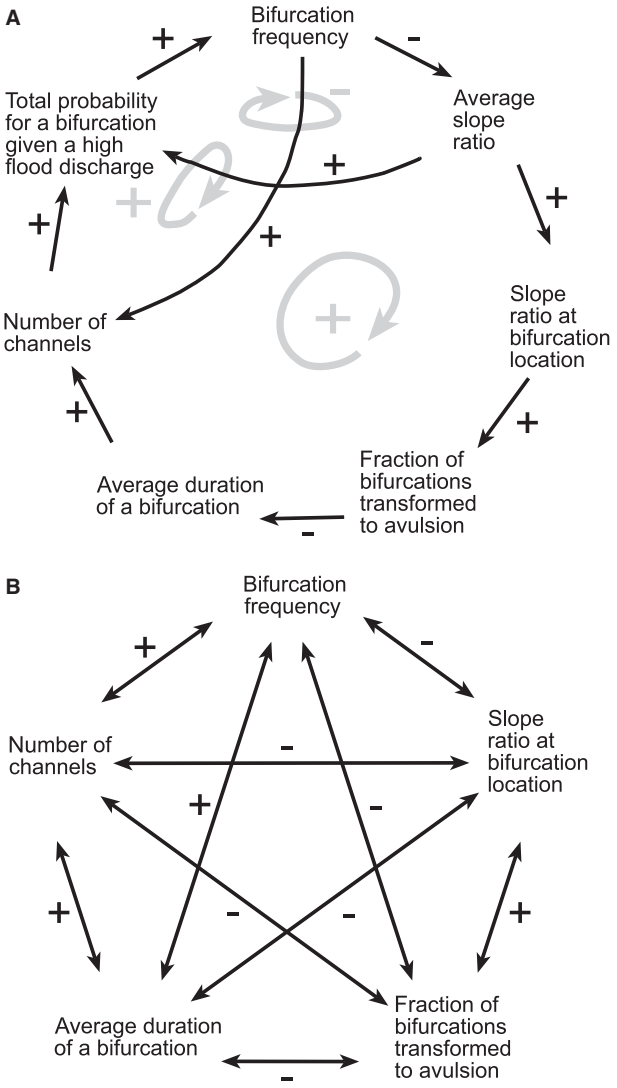


**Fig. 16.** Causal effects on model variables. Black arrows indicate positive (+) and negative (−) effects of one variable on another variable. (A) Direct effects. The network of effects contains two positive (+) and one negative (−) feedback loop, shown in grey. (B) Indirect effects derived from direct effects for variables included in the sensitivity analysis. Note that two negative effects have a net positive effect.

## Interaction between intrinsic processes

Figure 16A is a causal loop diagram (Ford, 1999) describing the interaction between the most important intrinsic factors in the evolution of the channel network. The magnitude of each of the factors, for instance the bifurcation frequency, changes over time as a result of three interacting feedback loops. The diagram shows two positive feedback loops and one negative feedback loop. A change in a factor in a positive feedback loop will amplify the impact of the change; a change in a factor in a negative feedback loop will reduce the impact of the change. Below, the relationships within each feedback loop are explained, starting at the total probability for a bifurcation ($P_{tot}$, Eq. 16).

The first relationship in the large positive feedback loop is the effect of the total probability for a bifurcation given a high flood discharge on bifurcation frequency, which is obviously positive because the frequency of bifurcations increases when the probability for a bifurcation increases. In turn, the bifurcation frequency has a negative effect on the average slope ratio because high bifurcation frequencies are associated with the short duration of the existence of channel belts and low channel-belt ridges. At a high average slope ratio, bifurcations will occur at higher slope ratios. At higher slope ratios at the bifurcation locations, a larger fraction of bifurcations will turn into (instant) avulsions, as explained in the previous section. When a larger fraction of bifurcations is transformed to avulsions, the average duration of bifurcations becomes smaller, which is a negative effect as indicated in Fig. 16A. A large average duration of bifurcations implies that many bifurcations are stable for a long time, resulting in a relatively stable channel network consisting of many channel belts. With an increasing number of channels,

 

the number of cells at the edge of channel belts ($n$ in Eq. 16) increases, resulting in an increase in the total probability for a bifurcation, given a high flood discharge.

The second positive feedback loop is shorter. The number of channels increases when a bifurcation occurs; so, bifurcation frequency has a positive effect on the number of channels. With an increasing number of channels, the number of cells at the edge of channel belts ($n$ in Eq. 16) increases, resulting in an increase in the total probability for a bifurcation. Finally, the total probability for a bifurcation has a positive effect on the bifurcation frequency, as explained above.

If these two positive feedback loops were the only feedback loops in place, a small initial increase in one factor, for instance average slope ratio, would result in a continuous increase or decrease in all other factors. There are two mechanisms that counteract this situation. The first mechanism is a negative feedback loop (Fig. 11). This loop consists of the positive effect of the total probability for a bifurcation on bifurcation frequency, the negative effect of bifurcation frequency on the average slope ratio and a positive effect of average slope ratio on the total probability for a bifurcation given a high flood discharge, explained by Eqs 10 and 16. These effects create the negative feedback loop which dampens the effect of the two positive feedback loops. The second mechanism that counteracts a continuous increase or decrease in factors in Fig. 16A is the removal of bifurcations that have been stable for a reasonable number of years. As discussed in the previous section, a bifurcation may be transformed into an unsuccessful bifurcation, or an avulsion, or a removed inflow channel bifurcation as a result of a large number of processes not shown in Fig. 16A. The result of such a removal is always a decrease in the number of channels.

An interesting question is how the effects in Fig. 16A can explain the variation in model outputs over periods between $0{\cdot}5 \times 10^3$ and $2 \times 10^3$ years (Figs 2, 7 and 11)? Firstly, the positive effect of the total probability for a bifurcation on bifurcation frequency is also observed in the model outputs: an increase in the total probability for a bifurcation given a high flood discharge is generally associated with an increase in the bifurcation frequency, which can be seen by comparing the D and F panels in Figs 2, 7 and 11. This positive effect is not always expressed in the model output because the relationship contains a probabilistic rule described above in the text that explains how Eq. 10 is used. Secondly, when the model output shows a longer duration of bifurcations, the number of channel belts on the floodplain also gets higher; this is, for instance, the case between $t = 2 \times 10^4$ and $4 \times 10^4$ in Fig. 2, representing a period with both a large duration of existence and a high bifurcation frequency compared with the rest of the model run. This relationship is explained by the positive effect of the average duration of a bifurcation on the number of channels (Fig. 16A). Finally, there is a strong positive relationship between the number of channels on the floodplain and the total probability for a bifurcation in the model, represented by a positive effect in Fig. 16A. Both variables show a marked cyclic variation over time, which is especially clear in the sediment supply scenario (Fig. 11). One cycle consists of a gradual increase in both variables, followed by an abrupt fall. This gradual increase is caused by the gradual increase in the number of channels on the floodplain, as a result of bifurcations. The abrupt fall is caused by the removal of a bifurcation that contains a large network of channels downstream of the branch of the bifurcation that is removed; this results in an abrupt fall in the number of channels, and an associated fall in the total probability for a bifurcation. This pattern repeats itself approximately five times in the realization of the sediment supply scenario shown in Fig. 11.

Other effects shown in Fig. 16A are less obvious in the model outputs. In addition, the duration between $0{\cdot}5 \times 10^3$ and $2 \times 10^3$ years of the period of variation in model output variables is hard to explain. It should be noted that the rates of change caused by each of the effects in Fig. 16A are important here, because each of these rates has an effect on how the system develops as a whole.

## SENSITIVITY ANALYSIS

### Methods

To study the effect of changes in parameters on floodplain dynamics, a sensitivity analysis was performed using the base-level rise scenario on the key input parameters of the model: floodplain aggradation exponent ($b$), critical discharge ratio ($u_{crit}$), slope ratio exponent ($\mu$), probability of a yearly flood discharge possibly leading to a bifurcation ($P(D)$). Model outputs considered were those that represent the floodplain dynamics: avulsion and bifurcation duration, avulsion

and bifurcation frequency, fraction of bifurcations that turns into an avulsion, number of coexisting channels and slope ratio at the bifurcation location. To estimate the probability distribution of these model outputs, 10 realizations of the model were created for each set of input parameter values. A larger number of realizations was not possible due to the long run time of the model. First, 10 realizations were created using input parameter values of the base scenario (Table 1). For each input parameter, the results of this base scenario acted as a reference for two other sets of runs, each consisting of 10 realizations, whereby the input parameter was decreased and increased in value, respectively. For each input parameter and for each output variable, this resulted in 10 realizations for each of the three different values of the input parameter, as shown in Fig. 17. The significance of changes in an output variable when an input parameter was changed was tested using a statistical test. For each pair of values of an input parameter, the null hypothesis that the mean values of the output variable are equal was tested. This procedure used a two-tailed bootstrap procedure with $\alpha = 0{\cdot}2$ (following Efron & Tibshirani, 1998).

## RESULTS

As could be expected due to the large difference in bifurcation frequency between two realizations (shown in Fig. 6), Fig. 17 shows that the range in the values of an output variable at a given input parameter value is large. In most cases, this range is larger than the change in the mean value of the output variable when the input parameter is increased or decreased. So, intrinsic controls cause a large range of possible model outcomes, even when input parameters are not changed.

Figure 17 shows that, for most of the input parameters, the applied change in the value of the input parameters has a significant effect on most output variables. Some effects of input parameter changes can be easily understood from knowledge of floodplain processes. At higher values of the overbank aggradation exponent ($b$), more aggradation of a channel belt is required to reach a super-elevation resulting in a high slope ratio and high probabilities for a bifurcation. As a result, an increase in $b$ results in a lower bifurcation and avulsion frequency. An increase in the critical discharge ratio $u_{crit}$ causes bifurcations to become less stable, resulting in a shorter bifurcation duration and, consequently, a smaller number of co-existing channels on the floodplain. An increase in the slope ratio exponent ($\mu$) results in an increase in the range of the values of the probability for a bifurcation because the slope ratio becomes either very low or very high. Due to the absence of intermediate values of the probability for a bifurcation when the slope ratio exponent is high, most bifurcations occur at high values of the slope ratio. Finally, increasing the probability for a high flood discharge P($D$) increases the bifurcation frequency.

The changes in the remaining output variables cannot directly be explained from knowledge of floodplain processes because these are due to indirect effects between output variables. These indirect effects can be derived from the direct effects in the causal loop diagram (Fig. 16A), resulting in a diagram (Fig. 16B) that shows positive and negative effects between most of the model output variables that are also shown in Fig. 17. When an input parameter value is changed, as shown in Fig. 17, the direction of change in an output variable relative to another output variable always corresponds to the sign of the indirect effect (Fig. 16B) between the two output variables: a positive indirect effect means that both output variables change in the same direction (both increase or decrease), and a negative effect means that they change in the opposite direction. This correspondence between the causal loop diagrams in Fig. 16 and the results of the sensitivity analysis confirms that the causal loop diagram (Fig. 16A) represents the main inter-relations between processes on the floodplain.

## CONCLUSIONS

A three-dimensional numerical model of sediment transport, erosion and deposition within a network of channel belts and an associated floodplain and hill slope is described. The model represents a substantial development of the Mackey & Bridge (1995) approach (the first numerical, 3D alluvial stratigraphy model), with completely new models for channel-belt and floodplain aggradation and degradation, channel-belt bifurcation and avulsion and the development of channel belts following avulsion. These model developments make it possible to investigate extrinsic (extrabasinal) controls on floodplain dynamics and alluvial architecture, and to assess fluvial sequence stratigraphy models.

Model input parameters were chosen based on data from the Rhine–Meuse delta. To examine

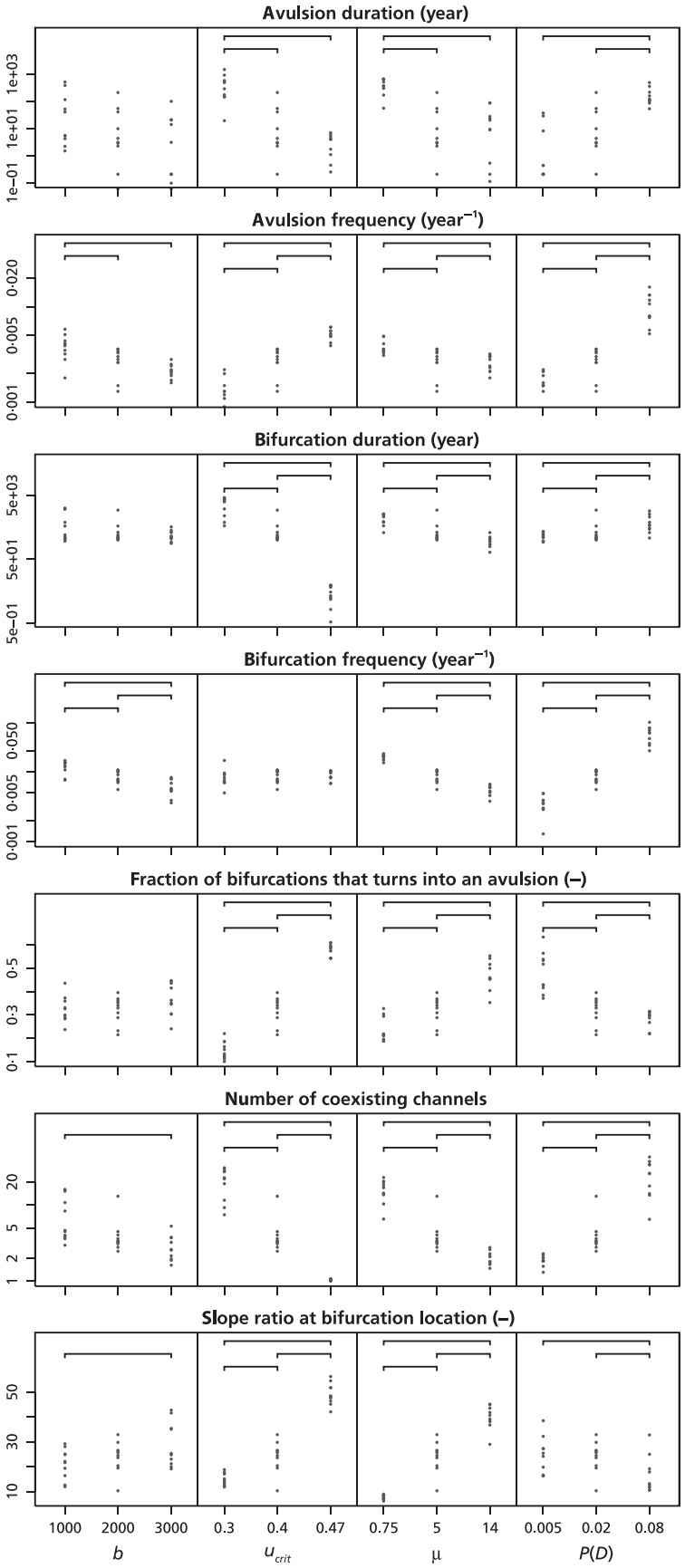


**Fig. 17.** Results of the sensitivity analysis. Each column provides the results of changing one parameter. Results are calculated for three parameter values: the value corresponding to the base scenario (Table 1), and one higher and one lower value. Each dot represents one realization. Horizontal bars connecting two parameter values indicate populations of outcomes that are significantly different (bootstrap procedure at $\alpha = 0{\cdot}2$). $b$ is the overbank aggradation exponent, $u_{\mathrm{crit}}$ the critical discharge ratio, $\mu$ the slope ratio exponent, $P_{\mathrm{tot}}$ the total probability for a bifurcation given a high flood discharge (Eq. 16).

how the model responds to extrinsic controls, the model was run under conditions of: (i) rising base level; (ii) falling then rising base level; and (iii) increasing sediment supply. Rises and falls in sea-level and increases in sediment supply occurred over 10 000 years. In scenario 1, a wave of aggradation moved up-valley in response to base-level rise, until aggradation occurred over the entire valley. The probability and frequency of bifurcations and avulsions (hence the number of coexisting channel belts) increased with the rate of sea-level rise and aggradation rate. Channel-belt width varied greatly due to differences in their water discharge and duration of existence. Wide, connected channel belts (and high channel-deposit proportion) occurred around the inflow point because of their high discharge and longevity. Less connected and smaller channel belts occurred further down-valley. This pattern of alluvial behaviour and architecture is also found in the Rhine–Meuse delta. During base-level fall (scenario 2), erosion and valley incision occurred, and the incised valley contained a single wide channel belt. During subsequent base-level rise, a wave of aggradation moved up-valley, and the incised valley was filled. Bifurcation and avulsion sites progressively moved upstream as in scenario 1. Relatively thin and narrow channel belts bordered and cut into the incised valley fill. These results differ substantially from existing sequence stratigraphy models. An increase in sediment supply from upstream (scenario 3) resulted in the development of an alluvial fan. Most bifurcations and avulsions occurred at the fan apex (nodal avulsion), and channel belts were widest and thickest here due to their high discharge and longevity. The fan apex is therefore a zone of high channel-deposit proportion. Width and thickness of channel belts decreased down-valley due to decreased discharge, longevity and aggradation rate. This behaviour occurs in modern alluvial fans.

Intrinsic controls also affect floodplain dynamics and alluvial architecture. Variation of aggradation rate, bifurcation frequency and number of coexisting channel belts occurred over periods of 500 to 2000 years. This variation is related to local aggradation and degradation of channel belts around bifurcation points, and complicated feedback among model variables. In addition, channel belts were preferentially clustered near floodplain margins, because of persistent low aggradation rate and topography there.

A sensitivity analysis was undertaken to show how model behaviour changes in response to changing key model input parameters. The next step is to simulate specific real-world examples in detail, by careful choice of input parameters, and allowing more input parameters to vary concurrently (e.g. base level, water and sediment supply, tectonic subsidence and uplift). This study represents the first attempt to examine the effects of both extrinsic and intrinsic controls on alluvial architecture using a numerical model. Although the numerical model represents a major improvement over the Mackey–Bridge approach, and explains many features of alluvial architecture observed in modern floodplains and alluvial fans, there is still room for improvement in the component mathematical models. Such improvement will only be achieved with further studies of the erosion and deposition, avulsion and alluvial architecture in modern fluvial environments. The effects on alluvial architecture of sediment compaction and syndepositional tectonism, considered in the Mackey–Bridge model, were not included here, but could easily be included in future.

## ACKNOWLEDGEMENTS

Donors of the American Chemical Society Petroleum Research Fund are acknowledged for support of this research. Additional support was provided by EC grant Eurodelta, EVK3-CT2001-20001. Cees Wesseling (PCRaster Environmental Software) and Kor de Jong are thanked for programming components of the model. Many people at the Department of Physical Geography, Utrecht University, have contributed with ideas and discussions related to the model, in particular Esther Stouthamer, the late Henk Berendsen, Maarten Kleinhans. Kim Cohen and two anonymous reviewers provided valuable comments on an earlier version of this manuscript.

## REFERENCES

**Allen, J.R.L.** (1978) Studies in fluviatile sedimentation: an exploratory quantitative model for architecture of avulsion-controlled alluvial suites. *Sed. Geol.*, **21,** 129–147.

**Allen, J.R.L.** (1979) Studies in fluviatile sedimentation: an elementary geometrical model for the connectedness of avulsion-related channel sand bodies. *Sed. Geol.*, **24,** 253–267.

**Ashworth, P.J., Best, J.L.** and **Jones, M.** (2004) The relationship between sediment supply and avulsion frequency in braided rivers. *Geology*, **32,** 21–24.

**Ashworth, P.J., Best, J.L.** and **Jones, M.** (2007) The relationship between channel avulsion, flow occupancy and aggradation in braided rivers: insights from an experimental model. *Sedimentology*, **54,** 497–513.

**Aslan, A., Autin, W.J.** and **Blum, M.D.** (2005) Late Holocene avulsion history of the Mississippi River, south Louisiana, U.S.A. *J. Sed. Res.*, **75,** 648–662.

**Berendsen, H.J.A.** and **Stouthamer, E.** (2001) *Paleogeographic Development of the Rhine–Meuse Delta, The Netherlands*. Koninklijke Van Gorcum, Assen, 268 pp.

**Blum, M.D.** and **Törnqvist, T.E.** (2000) Fluvial responses to climate and sea-level change: a review and look forward. *Sedimentology*, **47,** 2–48.

**Bridge, J.S.** (1999) Alluvial architecture of the Mississippi valley: predictions using a 3D simulation model. In: *Floodplains: Interdisciplinary Approaches* (Eds S.B. Marriott and J. Alexander), *Geol. Soc. London*, **163,** 269–278.

**Bridge, J.S.** (2003) *Rivers and Floodplains*. Blackwell, Oxford, UK, 491 pp.

**Bridge, J.S.** and **Leeder, M.R.** (1979) A simulation model of alluvial stratigraphy. *Sedimentology*, **26,** 617–644.

**Bridge, J.S.** and **Mackey, S.D.** (1993a) A revised alluvial stratigraphy model. In: *Alluvial Sedimentation* (Eds M. Marzo and C. Puidefabregas), *Int. Assoc. Sedimentol. Spec. Publ.*, **17,** 319–337.

**Bridge, J.S.** and **Mackey, S.D.** (1993b) A theoretical study of fluvial sandstone body dimensions. In: *Geological Modeling of Hydrocarbon Reservoirs* (Eds S.S. Flint and I.D. Bryant), *Int. Assoc. Sedimentol. Spec. Publ.*, **15,** 213–236.

**Bryant, M., Falk, P.** and **Paola, C.** (1995) Experimental-study of avulsion frequency and rate of deposition. *Geology*, **23,** 365–368.

**Burrough, P.A.** and **McDonnell, R.A.** (1998) *Principles of Geographical Information Systems*. Oxford University Press, Oxford.

**Chow, V.T., Maidment, D.R.** and **Mays, L.W.** (1988) *Applied Hydrology*. McGraw-Hill, New York.

**Cohen, K.** (2003) *Differential Subsidence within a Coastal Prism. Late Glacial Holocene Tectonics in the Rhine–Meuse Delta, The Netherlands*. Netherlands Geographical Studies, Utrecht, the Netherlands, 172 pp.

**Cohen, K.** (2005) 3D geostatistical interpolation and geological interpolation of palaeo-groundwater rise within the coastal prism in the Netherlands. In: *River Deltas: Concepts, Models, and Examples* (Eds L. Giosan and J.P. Bhattacharaya), *SEPM Spec. Publ.*, **83,** 341–364. SEPM (Society for Sedimentary Geology), Tulsa, OK.

**Efron, B.** and **Tibshirani, R.J.** (1998) *An Introduction to the Bootstrap*. Chapman & Hall/CRC, Boca Raton, FL.

**Ford, A.** (1999) *Modeling the Environment: an Introduction to System Dynamics Modeling of Environmental Systems*. Island Press, Washington, DC, 401 pp.

**Gouw, M.J.P.** and **Berendsen, H.J.A.** (2007) Variability of channel-belt dimensions and the consequences for alluvial architecture: observations from the Holocene Rhine–Meuse Delta (The Netherlands) and Lower Mississippi Valley (U.S.A.). *J. Sed. Res.*, **77,** 124–138.

**Gouw, M.J.P.** and **Erkens, G.** (2007) Architecture of the Holocene Rhine–Meuse delta (the Netherlands) – a result of changing external controls. *Neth. J. Geosci-Geol. Mijnbouw*, **86,** 23–54.

**Hancock, G.R., Willgoose, G.R.** and **Evans, K.G.** (2002) Testing of the SIBERIA landscape evolution model using the Tin Camp Creek, Northern Territory, Australia, field catchment. *Earth Surf. Proc. Land.*, **27,** 125–143.

**van Heijst, M.W.I.M.** and **Postma, G.** (2001) Fluvial response to sea-level changes: a quantitative analogue, experimental approach. *Basin Res.*, **13,** 269–292.

**Heller, P.L.** and **Paola, C.** (1996) Downstream changes in alluvial architecture: an exploration of controls on channel-stacking patterns. *J. Sed. Res.*, **66,** 297–306.

**Horn, B.K.P.** (1981) Hill shading and the reflectance map. *IEEE*, **69,** 14–47.

**Karssenberg, D.** and **Bridge, J.S.** (2005) A 3D model simulating sediment transport, erosion and deposition within a network of channel belts and an associated floodplain. In: *Eighth International Conference on Fluvial Sedimentology* (Eds G.J. Weltje, P. de Boer, J. VandenBerghe, K. van der Zwan, E. Stouthamer and H. Wolfert), p. 151. Delft, the Netherlands.

**Karssenberg, D.** and **De Jong, K.** (2005) Dynamic environmental modelling in GIS. 1. Modelling in three spatial dimensions. *Int. J. Geogr. Inf. Sci.*, **19,** 559–579.

**Karssenberg, D., Törnqvist, T.E.** and **Bridge, J.S.** (2001) Conditioning a process-based model of sedimentary architecture to well data. *J. Sed. Res.*, **71,** 868–879.

**Karssenberg, D., Bridge, J.S., Stouthamer, E., Kleinhans, M.G.** and **Berendsen, H.J.A.** (2003) Modelling cycles of fluvial aggradation and degradation using a process-based alluvial stratigraphy model. In: *Numerical and Physical Modelling of Sedimentary Systems, from Understanding to Prediction* (Eds P. de Boer, G. Postma, P. Kukla, C.J. Van der Zwan, P.M. Burgess, I. Ritsema and F. van den Belt), Utrecht, the Netherlands.

**Karssenberg, D., De Jong, K.** and **Van der Kwast, J.** (2007) Modelling landscape dynamics with Python. *Int. J. Geogr. Inf. Sci.*, **21,** 483–495.

**Leeder, M.R.** (1978) A quantitative stratigraphic model for alluvium with special reference to channel deposit density and interconnectedness. In: *Fluvial Sedimentology* (Ed. A.D. Miall), *Can. Soc. Petrol. Geol. Mem.*, **5,** 587–596.

**Mackey, S.D.** and **Bridge, J.S.** (1995) Three-dimensional model of alluvial stratigraphy: theory and application. *J. Sed. Res.*, **65,** 7–31.

**Makaske, B.** (2001) Anastomosing rivers: a review of their classification, origin and sedimentary products. *Earth-Sci. Rev.*, **53,** 149–196.

**Makaske, B., Berendsen, H.J.A.** and **Van Ree, M.H.M.** (2007) Middle Holocene avulsion-belt deposits in the central Rhine–Meuse Delta. *J. Sed. Res.*, **77,** 110–123.

**Meijer, X.D.** (2002) Modelling the drainage evolution of a river-shelf system forced by quaternary glacio-eustasy. *Basin Res.*, **14,** 361–377.

**Moore, I.D.** (1996) Hydrological modeling and GIS. In: *GIS and Environmental Modeling: Progress and Research Issues* (Eds M.F. Goodchild, L.T. Steyaert, B.O. Parsk, C. Johnston, D.R. Maidment, M.P. Crane and S. Glendinning), pp. 143–148. GIS World Books, Fort Collins, CO.

**Murray, A.B.** and **Paola, C.** (1994) A cellular model of braided rivers. *Nature*, **371,** 54–57.

**Overeem, I., Syvitski, J.P.M.** and **Hutton, E.W.H.** (2005) Three-dimensional numerical modeling of deltas. In: *River Deltas – Concepts, Models, and Examples* (Eds L. Giosan and J.P. Bhattacharya), *SEPM Spec. Publ.*, **83,** 13–30.

**Prosser, I.P.** and **Rustomji, P.** (2000) Sediment transport capacity relations for overland flow. *Prog. Phys. Geogr.*, **24,** 179–193.

**Schumm, S.A., Mosley, M.P.** and **Weaver, W.E.** (1987) *Experimental Fluvial Geomorphology*. Wiley, New York.

**Shanley, K.W.** and **McCabe, P.J.** (1993) Alluvial architecture in a sequence stratigraphic framework: a case history from

the Upper Cretaceous of southern Utah, USA. In: *The Geological Modeling of Hydrocarbon Reservoirs and Outcrop Analogues* (Eds S. Flint and I.D. Bryant), *Int. Assoc. Sedimentol. Spec. Publ.*, **15,** 21–56.

**Singh, H., Parkash, B.** and **Gohain, K.** (1993) Facies analysis of the Kosi Megafan deposits. *Sed. Geol.*, **85,** 87–113.

**Singh, V.P., Yang, C.T.** and **Deng, Z.Q.** (2003a) Downstream hydraulic geometry relations. 1. Theoretical development. *Water Resour. Res.*, **39,** SWC21–SWC215.

**Singh, V.P., Yang, C.T.** and **Deng, Z.Q.** (2003b) Downstream hydraulic geometry relations. 2. Calibration and testing. *Water Resour. Res.*, **39,** SWC31–SWC310.

**Slingerland, R.** and **Smith, N.D.** (1998) Necessary conditions for a meandering-river avulsion. *Geology*, **26,** 435–438.

**Smith, N.D., Cross, T.A., Dufficy, J.P.** and **Clough, S.R.** (1989) Anatomy of an avulsion. *Sedimentology*, **36,** 1–23.

**Smith, N.D., Slingerland, R.L., Perez-Arlucea, M.** and **Morozova, G.S.** (1998) The 1870s avulsion of the Saskatchewan River. *Can. J. Earth Sci.*, **35,** 453–466.

**Stouthamer, E.** and **Berendsen, H.J.A.** (2000) Factors controlling the Holocene avulsion history of the Rhine–Meuse delta (The Netherlands). *J. Sed. Res.*, **70,** 1051–1064.

**Stouthamer, E.** and **Berendsen, H.J.A.** (2001) Avulsion frequency, avulsion duration, and interavulsion period of Holocene channel belts in the Rhine–Meuse Delta, the Netherlands. *J. Sed. Res.*, **71,** 589–598.

**Stouthamer, E.** and **Berendsen, H.J.A.** (2007) Avulsion: the relative roles of autogenic and allogenic processes. *Sed. Geol.*, **198,** 309–325.

**Sun, T., Paola, C., Parker, G.** and **Meakin, P.** (2002) Fluvial fan deltas: linking channel processes with large-scale morphodynamics. *Water Resour. Res.*, **38,** 1151.

**Swenson, J.B.** and **Muto, T.** (2007) Response of coastal plain rivers to falling relative sea-level: allogenic controls on the aggradational phase. *Sedimentology*, **54,** 207–221.

**Törnqvist, T.E.** (1993) Holocene alternation of meandering and anastomosing fluvial systems in the Rhine–Meuse delta (central Netherlands) controlled by sea-level rise and subsoil erodibility. *J. Sed. Petrol.*, **63,** 683–693.

**Törnqvist, T.E.** (1994) Middle and Late Holocene avulsion history of the River Rhine (Rhine–Meuse delta, Netherlands). *Geology*, **22,** 711–714.

**Törnqvist, T.E.** and **Bridge, J.S.** (2002) Spatial variation of overbank aggradation rate and its influence on avulsion frequency. *Sedimentology*, **49,** 891–905.

**Tucker, G.E.** and **Whipple, K.X.** (2002) Topographic outcomes predicted by stream erosion models: sensitivity analysis and intermodel comparison. *J. Geophys. Res. B – Sol. Ea.*, **107,** 1–1.

**Van de Plassche, O.** (1995) Evolution of the intra-coastal tidal range in the Rhine–Meuse delta and Flevo Lagoon, 5700–3000 Yrs Cal BC. *Mar. Geol.*, **124,** 113–128.

**Wells, N.A.** and **Dorr, J.A.** (1987) Shifting of the Kosi River, northern India. *Geology*, **15,** 204–207.

**Whipple, K.X.** and **Tucker, G.E.** (2002) Implications of sediment-flux-dependent river incision models for landscape evolution. *J. Geophys. Res. B – Sol. Ea.*, **107,** 2039.

**Wright, V.P.** and **Marriott, S.B.** (1993) The sequence stratigraphy of fluvial depositional systems – the role of floodplain sediment storage. *Sed. Geol.*, **86,** 203–210.

## SUPPLEMENTARY MATERIAL

The following supplementary material is available for this article:

**Animation S1.** Base-level rise scenario, animation. Water discharge ($q_w$, $m^3$ $year^{-1}$) for each channel belt, area of channel belts and surface topography ($h$, m). Drag the slider to move backwards and forwards. (Right) click on animation for options.

**Animation S2.** Base-level fall–rise scenario, animation. Water discharge ($q_w$, $m^3$ $year^{-1}$) for each channel belt, area of channel belts and surface topography ($h$, m). Drag the slider to move backwards and forwards. (Right) click on animation for options.

**Animation S3.** Sediment supply scenario, animation. Water discharge ($q_w$, $m^3$ $year^{-1}$) for each channel belt, area of channel belts and surface topography ($h$, m). Drag the slider to move backwards and forwards. (Right) click on animation for options.

This material is available as part of the online article from http://www.blackwell-synergy.com/doi/abs/10.1111/j.1365-3091.2008.00965.x.

(This link will take you to the article abstract).

The animations are Flash files that can be viewed in a web browser with the Flash Player plugin installed. Click on the file name to open in a web browser. To open Flash files from hard disk, use the 'open file' dialogue of your web browser. Filenames:

**Animation S1:** S1BaseLevelRise.swf

**Animation S2:** S2BaseLevelFallRise.swf

**Animation S3:** S3SedimentSupply.swf

Please note: Blackwell Publishing is not responsible for the content or functionality of any supplementary materials supplied by the authors. Any queries (other than missing material) should be directed to the corresponding author for the article.

*Manuscript received 6 August 2007; revision accepted 4 March 2008*